X-RAY RESONANT RAMAN SCATTERING

SPECTRA SIMULATION FROM FIRST PRINCIPLES
FOR COPPER BELLOW IONIZATION THRESHOLD
USING HIGH-PERFORMANCE COMPUTING

GONÇALO GARCÊS SOBREIRA RODRIGUES BAPTISTA

BSc in Physics Engineering

DOCTORATE IN PHYSICS ENGINEERING

NOVA University Lisbon
September, 2023

X-RAY RESONANT RAMAN SCATTERING

SPECTRA SIMULATION FROM FIRST PRINCIPLES FOR COPPER BELLOW IONIZATION THRESHOLD USING HIGH-PERFORMANCE COMPUTING

GONÇALO GARCÊS SOBREIRA RODRIGUES BAPTISTA

BSc in Physics Engineering

Advisers: Jorge Felizardo Machado
Auxiliary Professor, NOVA University Lisbon

Mauro António Guerra
Auxiliary Professor, NOVA University Lisbon

Examination Committee

Chair: Name of the committee chairperson
Full Professor, FCT-NOVA

Rapporteur: Name of a rapporteur
Associate Professor, Another University

Members: Another member of the committee
Full Professor, Another University

Yet another member of the committee
Assistant Professor, Another University

DOCTORATE IN PHYSICS ENGINEERING

NOVA University Lisbon
September, 2023

X-ray resonant Raman scattering
Spectra simulation from first principles for Copper bellow ionization threshold using high-performance computing

Acknowledgements

Acknowledgments are personal text and should be a free expression of the author.

However, without any intention of conditioning the form or content of this text, I would like to add that it usually starts with academic thanks (instructors, etc.); then institutional thanks (Research Center, Department, Faculty, University, FCT / MEC scholarships, etc.) and, finally, the personal ones (friends, family, etc.).

But I insist that there are no fixed rules for this text, and it must, above all, express what the author feels.

," *Sometimes I'll start a sentence, and I don't even know where it's going.*
I just hope I find it along the way.
Like an improv conversation.
An improversation."

— **Michael Scott**, The Office
(Regional Manager of Dunder Mifflin Scranton)

"all work and no play makes Jack a dull boy   all work and no play makes Jack a dull boy
all work and no play makes Jack a dull boy   all work and no play makes Jack a dull boy
all work and no play makes Jack a dull boy   all work and no play makes Jack a dull boy
all work and no play makes Jack a dull boy   all work and no play makes Jack a dull boy
all work and no play makes Jack a dull boy   all work and no play makes Jack a dull boy
all work and no play makes Jack a dull boy   all work and no play makes Jack a dull boy
all work and no play makes Jack a dull boy   all work and no play makes Jack a dull boy
all work and no play makes Jack a dull boy   all work and no play makes Jack a dull boy
all work and no play makes Jack a dull boy   allworkandnoplaymakesJackadullboy
all work and no play makes Jack a dull boy   all work and no play makes Jack a dull boy
all work and no play makes Jack a dull boy   all work and no play makes Jack a dull boy
all work and no play makes Jack a dull boy   all work and no play makes Jack a dull boy
all work and no play makes Jack a dull boy   all work and no play makes Jack a dull boy
all work and no play makes Jack a dull boy   all work and no play makes Jack a dull boy
all work and no play makes Jack a dull boy   all work and no play makes Jack a dull boy
all work and no play makes Jack a dull boy   all work and no play makes Jack a dull boy
all work and no play makes Jack a dull boy   all work and no play makes Jack a dull boy
all work and no play makes Jack a dull boy   all work and no play makes Jack a dull boy
all work and no play makes Jack a dull boy   all work and no play makes Jack a dull boy
all work and no play makes Jack a dull boy   all work and no play makes Jack a dull boy
all work and no play makes Jack a dull boy   all work and no play makes Jack a dull boy
all work and no play makes Jack a dull boy   all work and no play makes Jack a dull boy
all work and no play makes Jack a dull boy   all work and no play makes Jack a dull boy
all work and no play makes Jack a dull boy   all work and no play makes Jack a dull boy
all work and no play makes Jack a dull boy   all work and no play makes Jack a dull boy
all work and no play makes Jack a dull boy   all work and no play makes Jack a dull boy
all work and no play makes Jack a dull boy   all work and no play makes Jack a dull boy
all work and no play makes Jack a dull boy   all work and no play makes Jack a dull boy
all work and no play makes Jack a dull boy   all work and no play makes Jack a dull boy
all work and no play makes Jack a dull boy   all work and no play makes Jack a dull boy
all work and no play makes Jack a dull boy   all work and no play makes Jack a dull boy
all work and no play makes Jack a dull boy   all work and no play makes Jack a dull boy
all work and no play makes Jack a dull boy   all work and no play makes Jack a dull boy
all work and no play makes Jack a dull boy   all work and no play makes Jack a dull boy
"

— **Jack Torrance**, The Shinning
(Caretaker of the Overlook)

v

Abstract

The work performed on this thesis comes as part of the effort to further understand the highly convoluted structure present on Copper's X-ray emission spectra, where, as with many other transition metals, a skewness can be observed on the $K_{\alpha_{1,2}}$, K_β and L transition lines. These lines originate due to the radiative relaxation of the atom's electronic structure post-ionization of inner shell electrons. However, it is very likely that the observed skewness is due to copper's satellite states' transitions.

Throughout this thesis, a study will be performed for the satellite states formed by the excitation of the inner-shell electrons, where, as opposed to the ionization process, usually considered in X-ray calculations, a photoexcitation process occurs.

Multiple atomic structure calculations will be performed using the *ab initio* state-of-the-art Multiconfiguration Dirac-Fock General Matrix Elements (*MCDFGME*) code for different excited states configurations.

The obtained results will then be used in the analysis of experimental data obtained from a High-Precision Double Crystal Spectrometer (DCS), using a synchrotron X-ray source.

Due to the complexity of the calculations, the process can become substantial in terms of computational power and time. Therefore, further similar and more complex studies will be performed by implementing and running a script in the *Oblivion* supercomputer located at the University of Évora.

Keywords: Atomic Excitation, X-ray lines, *MCDFGME*, DCS, High Performance Computing

Resumo

asdasdasdasd

Contents

Appendices

Annexes

List of Figures

List of Tables

Listings

Glossary

Feynman Diagram   2D diagram depicting various physical interactions between elementary particles. Fermions are depected as straight lines and bosons as wavy lines. *(p. 52)*

four-vector   Vector used in special relativity composed of 4 components, one scalar time-like, and three vectorial space-like. These vectors behave in special way, such as their norm being Lorentz invariant. Can be written in covariant, X_μ, and contravariant form, X^μ, with the difference being the sign of the time-like components. Example of a contravariant four vector: $X^\mu = (X^0, X^1, X^2, X^3) = (X^0, \boldsymbol{X})$ *(pp. xiv, 10)*

Lorentz invariant   A Lorentz invariant scalar, obtained, for example, from a Minkowski norm, does not change when operated by a Lorentz Transformation. *(pp. xiv, 10)*

Minkowski norm   Yields the Lorentz Invariant norm for a four-vector: $p_\mu p^\mu$. Equivalent to the dot product of a classical vector. *(pp. xiv, 10)*

self consistency method   The electron wavefunctions go through a variational process in order to reach convergence for an energetic minimum. *(p. 8)*

virtual photons   While in reality, during a Coulomb interaction, 'real' particles are not exchanged, the electromagnetic field is still mediated by photons. This way virtual photons are tools used in order to better represent electromagnetic interactions. *(p. 12)*

Acronyms

Grasp2k General-purpose Relativistic Atomic Structure Package 2k *(p. 14)*

MCDFGME Multiconfiguration Dirac-Fock General Matrix Elements *(pp. vi, viii, ix, 13–16, 19, 23, 24, 31–33, 41, 42)*

MCDF Multiconfiguration Dirac-Fock *(pp. viii, 12, 19)*

MPI Message Passing Interface *(pp. 21, 33, 40)*

DCS Double Crystal Spectrometer *(p. vi)*

EMF Electromagnetic Field *(pp. 7, 12, 18)*

FAC Flexible Atomic Code *(p. 14)*

HF Hartree-Fock *(p. 9)*

QED Quantum Electrodynamics *(pp. viii, 3, 12, 15, 19)*

Todo list

Theoretical Introduction

Throughout this thesis, different topics regarding Quantum Mechanics, Atomic Physics and spectroscopy will be approached, hence why a theoretical introduction is needed. In it, themes such as the characteristic X-rays of elements, the relativistic Dirac equation and QED corrections and methods for solving the many-body problem will be discussed.

> Falta introdução? Meter a conversa dos FP de 2008

1.1 Characteristic X-rays

When an atomic system is in a bound state, the electrons orbiting the nucleus are occupying fixed quantum states, defined by their principal atomic number, n, angular momentum, l, and spin, s. Electrons are also fermions, and thus must respect Pauli's exclusion principle, each occupying a single state, only occupied by that single electron. These quantum numbers provide information about each electron's wavefunction, and the collection of all the electrons' wavefunctions can be used in order to describe the whole system. When operating the Hamiltonian on this collection of wavefunctions, the atomic system's state's energy is obtained. Besides all the occupied states, an infinite more number of possible eigenfunctions will compose that system's base.

These bound systems, however tend to strive toward reaching an energetic minimum, associated with more stable states. Should the system be encountered in a state where energy is not minimize, it will eventually decay to a less energetic one.

When subjected to a high energy beam of particles (usually photons or electrons), an atomic bound system may go through the process of the ionization of inner-core electrons, which is followed by the emission of radiation of its own, in the form of X-rays and/or Auger electrons. The radiation emitted throughout this process presents well-defined energy values and thus provides a way to ascertain if an element is present in a sample under study. Due to this reason, these characteristic emissions are of an extremely high importance in a wide range of scientific areas.

1.1.1 Ionization as a vacancy generator

As previously mentioned, X-ray fluorescence spectroscopy has many uses and applications in a wide range of scientific areas. In this form of spectroscopy, the element at study, composed of a nucleus and N orbiting electrons, is bombarded with radiation leading to the ionization of inner-shell electrons while leaving a vacancy in their place (Figure 1.1).
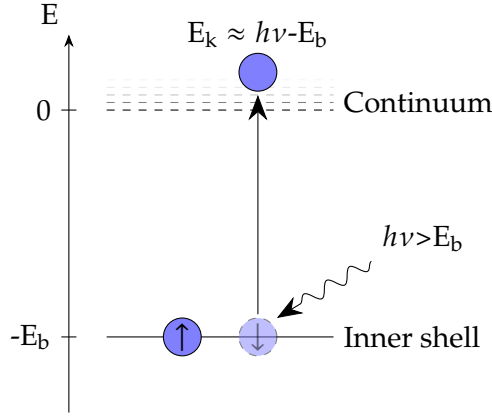
Figure 1.1: Photoionization.

The atomic structure, now composed of $N - 1$ electrons, will be left in an energetically unstable state, due to there being other possible lower energy states. This will lead to various processes of atomic relaxation, where the system will rearrange itself in order to find a lower energy configuration.

The main processes for this rearrangement are two competing decay paths: radiative relaxation, and Auger electron emission.

(a) Radiative Decay

(b) Auger Transition
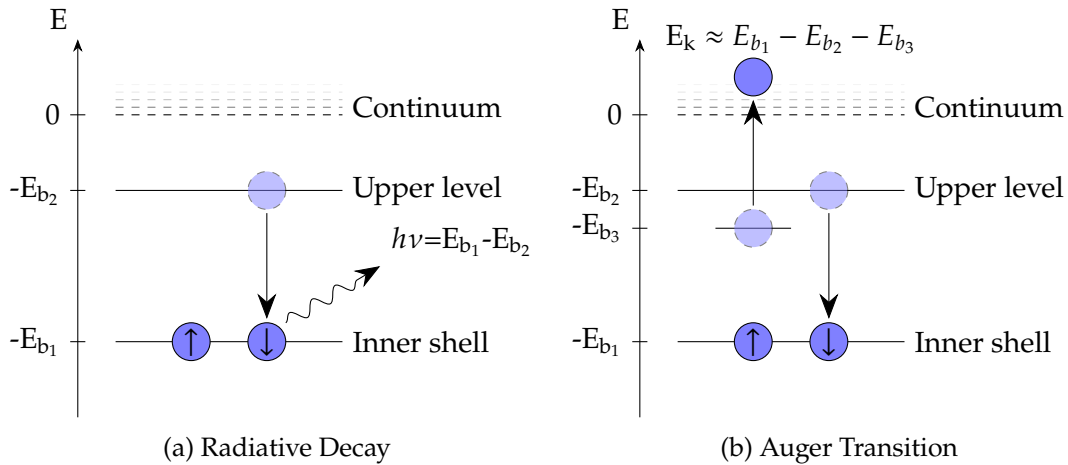
Figure 1.2: Principal atomic relaxation processes.

In the case of radiative relaxation, an upper shell electron will move and occupy the hole left in the inner shell. During this process, energy is released through the emission of photons with energy in the range of X-rays. The detection of these photons is what allows for an analysis and detection of the element at study.

On the other hand, an Auger emission occurs when in the process of an upper electron shifting to a shell hole, energy is released not in the form of photons, but by the atomic system going through the process of the ionization of a lesser bound electron.

In reality, when the initial vacancy is generated, two more processes can occur: shake-off and shake-up. Due to a sudden change in the potential felt by the remaining electrons, whilst going through the ionization, one other electron may become unbound, leading to a second ionization, the shake-off process, or may be excited to an upper state, during shake-up. These processes' occurrence probabilities are related to the rate at which the electron leaves the system during the first ionization. For lower electron emission energies, where the ionization process is rather "slow", and there is not much energy for shake up/off to occur, the adiabatic regime reigns. In this regime, the shake probabilities are small, and increase with the beam's energy. For higher energies, the transition occurs in the sudden regime, where the electrons' exit can be considered instantaneous. Now, while the shake probabilities still increase with the energy of the beam, they quickly saturate for a maxi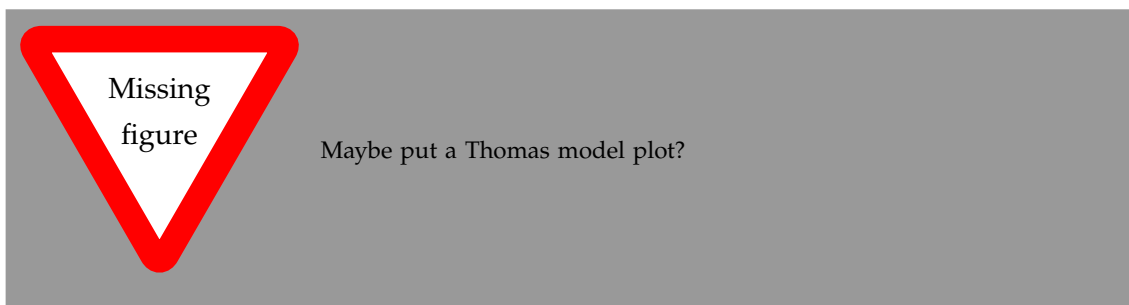mum value of probability, which can be calculated by computing overlaps between the electrons' initial and final states. These processes, however, are out of scope for this thesis, but should the reader be interested, the model conceived by Thomas [1] predicts the shake probability as a function of energy.

Missing figure

Maybe put a Thomas model plot?

1.1.2 Transition notation

The characteristic radiation measured from the radiative relaxation of a post-ionization unstable atomic system is one of the main ways of identifying an atomic element. This is due to the photons emitted possessing quantized values of energy, forming well-defined energy lines when observed in a spectrometer. In order to understand the change that occurred in the atomic system which lead to a specific emission, the spectral lines get labels based on a notation which usually takes into account the initial and final orbitals where the vacancy was present. A very illustrative diagram, exemplifying some transitions can be found in Appendix B.

Throughout this thesis, Siegbahn notation will be used, for the most part, but should the reader prefer IUPAC's, Table 1.1 has the conversion between notations.

Table 1.1: Siegbahn VS IUPAC notation. Adapted from [2].

Siegbahn	IUPAC	Siegbahn	IUPAC	Siegbahn	IUPAC
K_{α_1}	$K-L_3$	L_{α_1}	L_3-M_5	L_{γ_1}	L_2-N_4
K_{α_2}	$K-L_2$	L_{α_2}	L_3-M_4	L_{γ_2}	L_1-N_1
K_{β_1}	$K-M_3$	L_{β_1}	L_2-M_4	L_{γ_3}	L_1-N_2
$K_{\beta_2}^I$	$K-N_3$	L_{β_2}	L_3-N_5	L_{γ_4}	L_1-O_3
$K_{\beta_2}^{II}$	$K-N_2$	L_{β_3}	L_1-M_3	$L_{\gamma_4'}$	L_1-O_2
K_{β_3}	$K-M_2$	L_{β_4}	L_1-M_2	L_{γ_5}	L_2-N_1
$K_{\beta_4}^I$	$K-N_5$	L_{β_5}	$L_3-O_{4,5}$	L_{γ_5}	L_2-O_4
$K_{\beta_4}^{II}$	$K-N_4$	L_{β_6}	L_3-N_1	L_{γ_8}	L_2-O_1
$K_{\beta_4}^x$	$K-N_4$	L_{β_7}	L_3-O_1	$L_{\gamma_8'}$	$L_2-N_{5,6}$
$K_{\beta_5}^I$	$K-M_5$	L_{β_8}	$L_3-N_{6,7}$	L_η	L_2-M_1
$K_{\beta_4}^{II}$	$K-M_4$	L_{β_9}	L_1-M_5	L_l	L_3-M_1
		L_{β_9}	L_1-M_4	L_s	L_3-M_3
		L_{β_9}	L_3-N_4	L_t	L_3-M_2
		L_{β_9}	L_2-M_3	L_u	$L_3-N_{6,7}$
				L_v	$L_2-N_{6,7}$

1.1.3 Excitation as a vacancy generator

As previously mentioned, throughout this thesis, while the study is focused on the characteristic radiation emitted during an atomic relaxation process, the main vacancy generation method at study shall be the photoexcitation process (Figure 1.3), instead of ionization. The levels obtained after a photoexcitation of core shell electrons has occurred could be some of the many so-called satellite states, where the electronic configuration present during the relaxation process contains additional electrons or holes, or is simply not the standard configuration when talking about characteristic emissions. The characteristic radiation from transitions that originated from these states are one of the keys needed to fully comprehend and deconvolute an element's emission spectra.
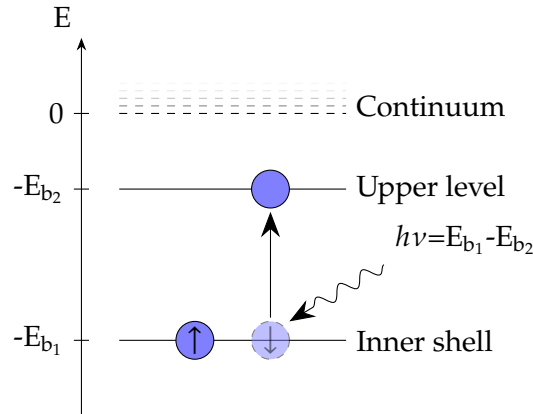

Figure 1.3: Resonant Photoexcitation

1.1.4 Radiative transitions

In terms of quantum mechanics, the properties of a system's change of state can be derived using perturbation theory, where a change in energy can be treated as perturbation, and takes into account the conservation laws physical properties, such as the angular momentum of the system as basis for the selection rules.

The transition's radiation type can be of two main flavors, Electric, E_k, or Magnetic, M_k, with k representing its multiplicity. These labels indicate which of the Electromagnetic Field (EMF) component had the strongest influence on the transition's occurrence. For both these types of transitions, the system's total angular momentum is allowed a change of $\Delta J = 0, \pm k$, and so does its projection, M_J. However, different transitions lead to different changes of parity in the system and to different selection rules.

It should also be of note that, usually, for the same multiplicity, an E transition is more intense than an M, and that it is also possible for rare 2-photon transitions to take place, where a combination of different transition types can occur.

The intensity of a transition is proportional to the squared norm of the perturbation's matrix element involving the initial and final state $\left(\Gamma_{if} \propto \left|\langle \psi_i | H' | \psi_f \rangle\right|^2\right)$. It should also be noted that the electron's initial state population will serve as a scaling factor for the transitions' rate. For example, while the transition rate for a $2p_{1/2} \rightarrow 1s$ and $2p_{3/2} \rightarrow 1s$ should be about the same, the orbital $2p_{3/2}$ has double the population $2p_{1/2}$ has, hence why the K_{α_2} line has about half the K_{α_1} line's intensity.

One should also mention that monochromatic transitions do not exist. While the transition might have a well-defined energy, calculated by the difference in energy between the initial and final levels, due to Heisenberg's uncertainty principle, $\Delta E \Delta t > \frac{\hbar}{2}$, there will exist a natural energy broadening proportional to the decay rate, $\Gamma = \hbar R$, the transition's natural width. The shapes representing these transitions are given by a Lorentzian distribution.

1.2 Solving the atomic many-body problem

When studying a system composed of multiple charged bodies, one must consider all the existing interactions. Whilst there are known analytical solutions for 2-bodies Hydrogenoid systems, with the presence of more non spatially-bound particles, the Coulomb interaction pairs lead to the impossibility of finding a set of analytical wavefunctions which are a part of the Hamiltonian's eigenset. Consecutively, the need for a numerical method that is able to compute solutions for these complex systems arose.

1.2.1 The non-relativistic Hamiltonian

The first approach used in order to solve the many-bodies problem used a non-relativistic consideration. This way, the Hamiltonian consists on the sum of the system's non-relativistic momentum-related energies and the energy of Coulomb interactions

between all the bodies in the system, while considering the nucleus as fixed in space, due to it being thousands of times more massive than the orbiting electrons.

Essentially, and in atomic units:

$$\sum_i^N \overbrace{\frac{1}{2}\nabla_i^2}^{E_1} \overbrace{-\frac{Z}{r_i}}^{E_2} + \underbrace{\sum_{i<j}^{j} \overbrace{\frac{1}{r_{ij}}}^{E_3}}_{\text{Pair repulsion}} ,$$

$$\underbrace{\phantom{\sum_i^N \frac{1}{2}\nabla_i^2 -\frac{Z}{r_i}}}_{\text{Individual Hamiltonian}}$$

$$E_1 \rightarrow \text{Momentum} \quad E_2 \rightarrow \text{e}^-\text{nuc. Coulomb attraction} \quad E_3 \rightarrow \text{e}^-\text{e}^- \text{ Coulomb repulsion}$$
$$(1.1)$$

1.2.2   The Hartree-Fock Method

This numerical method is one of the staple and most enduring procedures for solving the problem associated with a many-body system. As a side note, an in-depth explanation on all the intricacies of this method can be found in many of the literature, but as for the writing of this thesis, the works [3–6] were the ones consulted.

Hartree developed an iterative method, further enhanced by Fock and Slater, based on the field's self consistency method. In this approach, when studying a multi-electronic system, such as an atom, each electron's wavefuction is composed as a product of a spacial part, ψ, and one related to the electron's spin, χ, which can be used for the calculation of relativistic effects.

$$u = \psi\chi, \tag{1.2}$$

The wavefuction capable of describing the whole system, Ψ, should be somewhat of a product of all the wavefunctions describing each individual electron. However, one must not forget the need for this wavefunction to respect the antisymmetry principle, due to the electron's fermionic nature. In order to achieve this, Ψ is to be composed of a Slater determinant, as to also be able to account for Pauli's exclusion principle:

$$\Psi = \frac{1}{\sqrt{N!}} \begin{vmatrix} u_1(x_1) & u_2(x_1) & \cdots & u_N(x_1) \\ u_1(x_2) & u_2(x_2) & \cdots & u_N(x_2) \\ \vdots & \vdots & \ddots & \vdots \\ u_1(x_N) & u_2(x_N) & \cdots & u_N(x_N) \end{vmatrix} . \tag{1.3}$$

It is of high importance that the set of basis wavefunctions respects orthonormality. These are to be initialized as trial wavefunctions for the numerical method.

The main goal for this algorithm is to, as per the self consistency method, follow the variational principle with the goal of minimizing a functional, as a way of reaching an energetic minimum. This optimal, yet unknown energy, E_0 (calculated by operating the Hamiltonian on the system's optimal wavefunctions), will attempt to be reached by the

[margin note: Explain antisymmetry and put it in the glossary**]**

[margin note: Explain in the glossary**]**

variation of the trial wavefunctions that provide a non-minimized solution. Whilst the optimal wavefunctions will never be reached, the purpose of this method is to reach a solution that yields an energetic value as close as possible to E_0, while always yielding $\langle \Psi | H | \Psi \rangle \geq E_0$, due to the numerical nature of the method.

The computational method consists on starting with the previously mentioned trial wavefunctions and employing them in the Hartree-Fock's potential calculation through the Hartree-Fock (HF) equations.

In a simplified scheme, the self-consistent Hartree-Fock computational method can be represented by the block diagram in Figure 1.4.

Finish the explanation

Figure 1.4: HF method's block diagram.
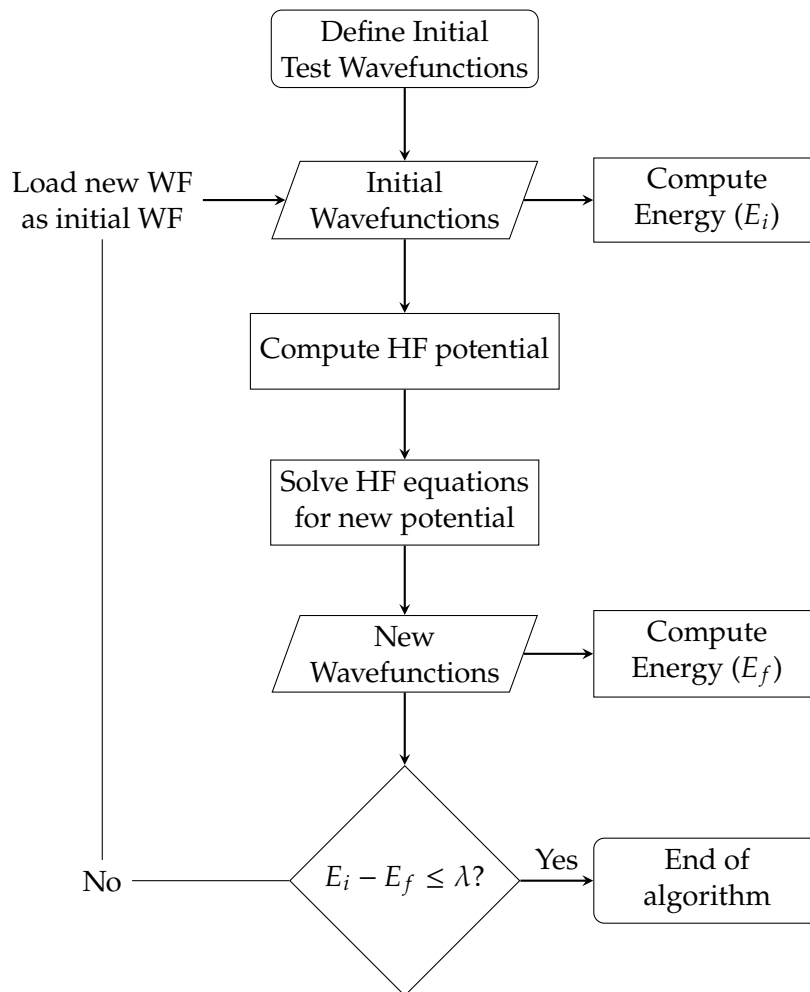
1.2.3 The Dirac Equation

While Schrödinger's equation may be one of the most significant and impactful equations in Modern Physics, it is also not free of its of limitations. The fact that it does not account for the existence of the electron's spin and the lack of consideration of relativistic effects are some of the most impactful setbacks. Consulting the works in [7–10], this

work will follow an exploration of different approaches that followed in order to solve the aforementioned problem.

Many scientists, such as Klein, Gordon and later Fock, had already conceived a relativistic correction to Schrödinger's equation, where the free-particle energy makes use of the relativistic momentum-energy relation, as displayed in equation (1.4).

$$E = \sqrt{c^2 p^2 + m^2 c^4}, \tag{1.4}$$

This notable definition can be derived from the Lorentz invariant scalar produced by Minkowski norm of the momentum four-vector (1.5).

$$p^\mu p_\mu = m^2 c^2 \Leftrightarrow \frac{E^2}{c^2} - p^2 = m^2 c^2 \Leftrightarrow \frac{E^2}{c^2} = p^2 + m^2 c^2, \tag{1.5}$$

Now, inputting this new energy operator into Schrödinger's equation, yields the Klein-Gordon equation (1.6), allowing for Schrödinger's equation to now be Lorentz-invariant (proof can be found in Strickland's book [11]).

$$-\hbar^2 \frac{\partial^2}{\partial t^2} \psi = \left(-c^2 \hbar^2 \nabla^2 + m^2 c^4 \right) \psi, \tag{1.6}$$

This new approach was, however, still limited, as it only described spin 0 particles (e.g., some mesons), and made use of a second order derivative in the time-like component.

Came 1928 and a new equation was developed by Paul Dirac [12], one taking now into account not the classical 3 dimensional space components, but the relativistic four components.

Dirac started by rewriting the energy-momentum relation, ending up with an equivalent equation (1.7), employing 4×4 matrices, due to the 4 relativistic dimensions at play, and incorporating spins into the equation by making use of the Pauli matrices (1.9).

$$E = c\boldsymbol{\alpha} \cdot \boldsymbol{p} + \beta m c^2, \quad \boldsymbol{\alpha} = (\alpha_1, \alpha_2, \alpha_3), \tag{1.7}$$

$$\alpha_i = \begin{pmatrix} 0 & \sigma_i \\ \sigma_i & 0 \end{pmatrix} \qquad \beta = \begin{pmatrix} I_2 & 0 \\ 0 & -I_2 \end{pmatrix} \qquad I_2 = \begin{pmatrix} 1 & 0 \\ 0 & 1 \end{pmatrix}, \tag{1.8}$$

$$\sigma_1 = \begin{pmatrix} 0 & 1 \\ 1 & 0 \end{pmatrix} \qquad \sigma_2 = \begin{pmatrix} 0 & -i \\ i & 0 \end{pmatrix} \qquad \sigma_3 = \begin{pmatrix} 1 & 0 \\ 0 & -1 \end{pmatrix}, \tag{1.9}$$

In order to fully comprehend this shift of notation, one should equate the square of the two equations, (1.4) and (1.7), and confirm its validity.

$$c^2 p^2 + m^2 c^4 = c^2 \boldsymbol{\alpha}^2 p^2 + 2mc^3 \boldsymbol{\alpha} \cdot \boldsymbol{p} \cdot \beta + \beta^2 m^2 c^4, \tag{1.10}$$

In order for this equation to make sense, the following conditions must be true (which in fact, they are):

Try to explain why this might be a problem

do the demonstration, dummy

$$\begin{cases} c^2 p^2 = c^2 \alpha^2 p^2 & \Leftrightarrow \alpha^2 = 1 \\ 0 = 2mc^3 p \alpha \beta & \Leftrightarrow \alpha \beta = 0 \ , \\ m^2 c^4 = \beta^2 m^2 c^4 & \Leftrightarrow \beta^2 = 1 \end{cases} \qquad (1.11)$$

Taking the previous considerations into account, one can now construct Dirac's free-particle equation (1.12):

$$i\hbar \frac{\partial}{\partial t} \psi = \left(c\boldsymbol{\alpha} \cdot \boldsymbol{p} + \beta mc^2 \right) \psi = \begin{pmatrix} mc^2 I_2 & -i\hbar c \boldsymbol{\sigma} \cdot \nabla \\ -i\hbar c \boldsymbol{\sigma} \cdot \nabla & -mc^2 I_2 \end{pmatrix} \cdot \begin{pmatrix} \psi_1 \\ \vdots \\ \psi_4 \end{pmatrix}, \qquad (1.12)$$

This equation, however, as mentioned above, can only describe a single particle present in a field-free region. In order to account for the existence of a field, such as the electromagnetic field, derived from the four-potential A^μ, composed by the electric scalar potential field, $A^0 = \phi$, and the vector potential, $(A^1, A^2, A^3) = \boldsymbol{A}$, the following change on the momentum four-vector must be made:

$$p^\mu \rightarrow p^\mu - eA^\mu, \quad A^\mu = (\phi, \boldsymbol{A}), \qquad (1.13)$$

The Hamiltonian can now be rewritten as to account for the presence of the electromagnetic field (1.14). This way it is possible to include, for example, the electron-nucleus Coulomb attraction.

$$H_D = -e\phi + \beta mc^2 + \boldsymbol{\alpha}(c\boldsymbol{p} + e\boldsymbol{A}), \qquad (1.14)$$

For a central fixed potential, as is the one generated by the nuclear charge, the 3 space-like components from the four-potential are null, and the time-like component, $\phi = \dfrac{Ze}{r}$. The Hamiltonian gains now a more recognizable form:

$$H_D = -\frac{e^2 Z}{r} + \beta mc^2 + \boldsymbol{\alpha} \cdot \boldsymbol{p}c, \qquad (1.15)$$

A very interesting fact about Dirac's equation is that it yields, in fact, two-component solutions: the large component (positive energy values), for particles, and the small component (negative energy values), for antiparticles.

1.2.3.1 The Dirac-Breit Equation

Once again, when considering a system composed of many bodies, one must consider all the present interactions, namely, the electron-electron repulsion in an atom. Breit, in 1929, had created a relativistic approach to treat the electron-electron interactions, consisting on a set of equations building upon the classical non-relativistic Hamiltonian from equation (1.1), which can be consulted in Appendix A. Breit's equations are able to

account for angular momenta couplings and estimate level energy splittings, the change of a particle's apparent mass as a function of velocity, and even include the interaction of an applied external magnetic field [10].

It is quite obvious Breit's equations introduce a great complexity in the search of the new Hamiltonian's eigenfunctions. Nonetheless, when trying to include an approximation of Breit's considerations into Dirac's equation, one must add the following operator to the one present in equation (1.15):

$$H_B = \sum_{i>j} \frac{e^2}{r_{ij}} - e^2 \left(\frac{\boldsymbol{\alpha}_i \boldsymbol{\alpha}_j}{r_{ij}} + \frac{(\boldsymbol{\alpha}_i \boldsymbol{\nabla}_i)(\boldsymbol{\alpha}_j \boldsymbol{\nabla}_j) r_{ij}}{2} \right), \tag{1.16}$$

This set of terms will account for the fact that Coulomb interactions, mediated by the electric field, and therefore, virtual photons, cannot occur at instantaneous velocities, but at the speed of light.

1.3 QED considerations

Lorem ipsum dolor sit amet, consectetur adipiscing elit. Etiam ut justo justo. Cras pulvinar massa sollicitudin ligula faucibus, in vulputate magna viverra. Nulla risus ante, maximus ut nunc sit amet, condimentum convallis mi. Phasellus et mi aliquet, ornare sapien egestas, vehicula orci. Donec ac massa tempus, iaculis tortor vitae, tempus tortor. Donec nec justo eros. Sed mauris purus, facilisis eu tempus quis, mattis et erat. Sed et congue metus, in venenatis nibh. Nullam ipsum ex, scelerisque non nunc sit amet, ultrices commodo felis. Proin sodales turpis nulla, quis tincidunt leo auctor id. Ut ac nulla quis felis molestie ullamcorper. Nulla tristique dui velit, sit amet rutrum libero dignissim id.

In hac habitasse platea dictumst. Vivamus laoreet neque odio, vitae faucibus massa eleifend sit amet. Curabitur tempor facilisis velit, eget blandit nisi rutrum at. Morbi a massa a lacus lobortis ultricies eget vel enim. Ut augue nisl, tristique eget luctus eget, scelerisque vitae risus. Aliquam in felis et metus euismod porttitor. Nullam nec ligula mi. Aliquam non vulputate sem. Proin ut leo eget ex bibendum venenatis ac vel sapien. Cras felis eros, cursus quis dolor posuere, scelerisque tempus orci. In nec quam in dui efficitur aliquam vitae sit amet dui. Cras laoreet tellus vel risus molestie mattis. Nulla facilisi. Duis rutrum mauris vitae malesuada consequat.

Should the atomic system be subjected to an external EMF, the level structure would change due to Zeeman's and Stark's effects, allowing for the probing of the atom's hyperfine structure.

1.3.1 The *MCDF* Method

As previously mentioned in section 1.2.2, there is a need for a numerical method in order to compute and find the eigenfunctions for a many-body Hamiltonian. While the Hartree-Fock method was able to reasonably solve the non-relativistic problem, now,

Falar aqui sobre as contribuições. Não tem que ser extensivo

Ler bem o manual e explicar bem o método e todas as coisas diferentes que se podem fazer
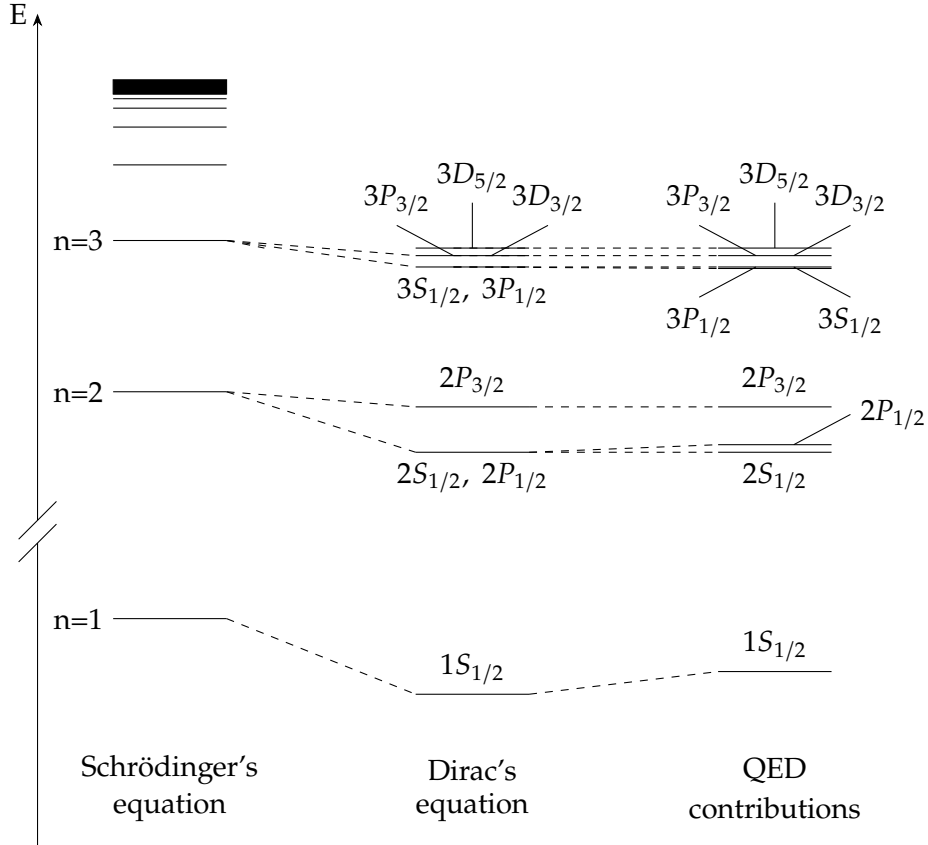
Figure 1.5: Comparison of Hydrogen level diagrams. Adapted from [13]

while considering the Dirac-Breit Hamiltonian from equations (1.15) and (1.16), there is a need for a new method.

Hence, the state of the art *MCDFGME* arises. This self-consistent iterative method, based on the same method present in section 1.2.2, is able to solve and find eigenfunctions for a multielectronic system, now taking into account the Dirac-Breit Hamiltonian. Moreover, it is also capable of incorporating electron correlation and many QED effects not yet considered in the relativistic equation, such as the Lamb-shift, vacuum polarization, and the electron's self energy. A brief description of these contributions can be found in appendix C

1.4 State-of-the-Art

This really needs a re-do

In this section, an overview of the most up-to-date research regarding the previous topics applied to the main subject of interest of this thesis, Copper K_α x-ray transitions and atomic structure calculations will be discussed.

1.4.1 Copper's characteristic X-rays

Copper is a dominant element in today's society. While most of its uses are day-to-day related, it also has a high prevalence in many physical areas, namely, copper's K_α transitions [14]. While these radiative transitions have been measured countless times, with very well recorded energy values [15–19]. It is also common knowledge Copper's K_α lines do not have a symmetric distribution, since both K_{α_1} and K_{α_2} line display a negative (left-tailed) skewness. Due to this fact, most of the fitting models used in order to analyze both Copper's K_{α_1} and K_{α_2} transitions involve the usage of a Lorentzian doublet, for each line [20, 21]. While many associate these asymmetries due to satellite states formed by shake processes [14, 22], with some theoretical studies having been performed [23], some authors note it could be due to X-ray resonant Raman scattering [22]. This effect occurs when a sample is exposed to energies under to near the ionization threshold, when a bound electron is excited to an upper state [24]. While there are some studies exploring this topic, most are focused on the cascade of low energy transitions that follow the post-scattering excitation [25]. Nonetheless, a previous experimental study has been able to show that for Copper exposed to synchrotron radiation tuned to energies near K-shell's ionization energy, some K_{α_1} transitions demonstrated to be narrower than expected [26].

1.4.2 MCDFGME capabilities

It has been noted multiple times that *MCDFGME* code excels in atomic structure calculations of super-heavy elements and highly-charged ions, where relativistic and QED effects are in prevalence [27–29]. However, it has also been proven to be an excellent tool for the calculation of less ionized and lighter atomic systems [30].

In addition, the *MCDFGME* code is able to calculate radiative and auger transition rates for the calculated configurations, which can be used in the simulation of theoretical spectra, due to being able to compute the transition's intensity and natural width. Since it is able to perform calculations, even for exotic atoms, it can be used to further understand many QED phenomena, further exploring the limits of our theory, and it's comparison to experimental data [31].

It should also be of note that there are many other code alternatives. While *MCDFGME*, which is a close-source project, provides a very high precision in the performed calculations at a high computational cost, Flexible Atomic Code (FAC), is an open source code which requires less computational time for the calculations, however, it lacks *MCDFGME*'s precision, since it only is able to consider all the spin-orb couplings, but does not mix the possible configurations originating them. It can, however, calculate other collisional processes, such as electronic impact excitation cross-sections [32]. General-purpose Relativistic Atomic Structure Package 2k (*Grasp2k*) [33], and *AUTOSTRUCTURE* [34] are other codes with some of the same capabilities.

Atomic Structure Calculations

In this chapter, the procedure that follows a standard atomic structure calculation will be discussed and explained in detail. Topics ranging from the usage of the *MCDFGME* code to compute quantities such as energy levels, orbital wavefunctions and transition rates, to the manner in which these parameters can be used in order to simulate a theoretical spectrum will be explored. All the information present in this chapter was obtained after a thorough study of *MCDFGME*'s manual [35].

2.1 The *MCDFGME* code's capabilities

As previously stated, *MCDFGME* is a program that allows for not only solving the many-body problem for an atomic system while making the proper QED energy corrections, but also for the computation of a great deal of atomic parameters. Consulting [36], one can see that these include, but are not limited to:

- Energy level calculations.

- Multipole radiative transition probabilities.

- Auger transition probabilities.

- Photoionization cross-sections.

- Electronic impact excitation cross-sections.

- Orbital wavefunction overlaps between same and different atomic systems.

meter mais cenas

2.2 The atomic system at study

Before proceeding to the explanation behind every step of the calculations performed, a previous discussion on the reason behind them should be had.

The main purpose of this thesis is that of simulating a theoretical spectrum for Copper's x-ray emission lines when subjected to a near ionization threshold x-ray source.

At this energy range, two main processes will be responsible for an electron moving out of a core-shell: Resonant photoexcitation, and ionization.

While the simulation of the theoretical spectra for ionized Copper would be quite straightforward (due to the low shake probabilities at near ionization threshold energies, transitions for satellite states were not incorporated in the simulation), the more extensive calculation is that of resonant photoexcitation.

Aside from ionized Copper, multiple atomic structure calculations were performed for many of Copper's first excited state configurations in order to consistently account for all possible decays from excited states.

In total, and in addition to ionized Copper, 18 different standalone calculations were performed for the case in which the atomic system has undergone the process of an excitation of any one of the constituent electrons to one of the following orbitals:

- 4s, 4p, 4d, 4f

- 5s, 5p, 5d, 5f, 5g

- 6s, 6p, 6d, 6f, 6g, 6h

- 7p, 8p, 9p

2.2.1 Selecting all possible orbital configurations

As to perform an atomic structure calculation, by making use of the *MCDFGME* code, the system's electronic configuration is needed, hence why, for each calculation, all the possible one-hole and two-holes [1] configurations need to be provided, along with their respective labels which are used as identifiers of the orbital where the hole is present during the calculations. For example, in the case of ground state Copper that went through the process of the excitation of one of its electrons to the orbital 4p, there are many possibilities for the original orbital from where the electron came from. For this case, an example of all possible 1-hole and 2-holes configurations can be found in Annex I. These are obtained by running a single hole, or two holes by all the orbitals present in the ground state configuration.

2.3 Level Calculations

Now that all configurations have been selected, the calculations can proceed.

The first and most influential, step needed in order to simulate theoretical spectra is the calculation of the level structure for all given configurations.

---

[1]These need to be considered due to describing the final state of the system after an Auger transition or Shake-off process. The Auger transition rates will be needed in order to compute the full width of the initial 1-hole level and diagram transitions.

This, however, is no simple task. Besides the given configuration, an atomic level is described by two other quantum numbers.

2.3.1 The level manifold

Prior to proceeding with the discussion, it is important to establish some of the notation that will be used throughout this thesis. In this work, where hyperfine splitting is not accounted for, an atomic level will be described by three sets of quantum numbers. These will be the parameters that will influence the system's energy levels.

Hole orbital labels $\left(n\, l_j\right)$ - This quantum number set is related to the system's electronic configuration and can be composed of one or more labels, indicators of the orbitals where electrons are missing. These labels may have no physical meaning on their own and are used in conjunction with files such as the one in Annex I in order to retrieve the system's electronic configuration. For demonstrative purposes, assuming an initial Copper's ground state configuration as a starting point, before any hole-generating processes, to be $1s^2\, 2s^2\, 2p^6\, 3s^2\, 3p^6\, 3d^{10}\, 4s^1$, the quantum number set in question can be used to describe various possible ionization configurations:

- $1s^1\, 2s^2\, 2p^6\, 3s^2\, 3p^6\, 3d^{10}\, 4s^1 \rightarrow (1s)$

- $1s^1\, 2s^1\, 2p^6\, 3s^2\, 3p^6\, 3d^{10}\, 4s^1 \rightarrow (1s, 2s)$

Total angular momentum number J - This number is the indicator of the total angular momentum of the atomic system, resulting from the couplings between the electrons' orbital angular momenta and spin. A single configuration can result in many coupling possibilities and, in turn, different values for J.

As an example, let's take that of Copper that underwent the excitation process of an electron from the 2p orbital to 4p, with an electron configuration of $1s^2\, 2s^2\, 2p^5\, 3s^2\, 3p^6\, 3d^{10}\, 4s^1\, 4p^1$. One can now easily observe there are three open orbitals, each with an uncoupled electron. The different coupling possibilities between these three electrons will generate four different possible total angular momentum values: $J = {}^1\!/_2,\ {}^3\!/_2,\ {}^5\!/_2,\ {}^7\!/_2$. In table 2.1, a coupling example will be given for each of them.

Table 2.1: Total angular momentum generated by different couplings. The indicated orbital refers to where a hole is present.

2p		4s		4p		Total/J
M_l	M_s	M_l	M_s	M_l	M_s	$M_l + M_s$
1	$-{}^1\!/_2$	0	$-{}^1\!/_2$	1	$-{}^1\!/_2$	${}^1\!/_2$
1	${}^1\!/_2$	0	$-{}^1\!/_2$	1	$-{}^1\!/_2$	${}^3\!/_2$
1	${}^1\!/_2$	0	${}^1\!/_2$	1	$-{}^1\!/_2$	${}^5\!/_2$
1	${}^1\!/_2$	0	${}^1\!/_2$	1	${}^1\!/_2$	${}^7\!/_2$

Lagrange multiplier ϵ - Indicator of the eigenvalue for the state on which the calculation will be performed on. The need for this quantum number arises from the fact that, even for the same configuration and the same total angular momentum, there are many possible arrangements that yield these quantum numbers. The total wavefuction will be composed as linear combination with mixing coefficients for each level with different ϵ. As an example, for the same configuration used previously, and assuming a total angular momentum $J = {}^5/_2$, there are three different possible couplings that generate that value of angular momentum, as can be seen in table 2.2.

Table 2.2: Same total angular momentum generated by different configurations

$J = {}^5/_2$					
2p		4s		4p	
M_l	M_s	M_l	M_s	M_l	M_s
1	$-{}^1/_2$	0	${}^1/_2$	1	${}^1/_2$
1	${}^1/_2$	0	$-{}^1/_2$	1	${}^1/_2$
1	${}^1/_2$	0	${}^1/_2$	1	$-{}^1/_2$

This splitting of quantum numbers for a given configuration gives origin to the level manifold (Figure 2.1), reason why, even for a simple calculation, hundreds to thousands of levels need to be calculated. It is also of note that, for a given Total angular momentum value, J, there are $2J + 1$ states associated to it due to the angular momentum projection. In the presence of an external EMF, the hyperfine level structure would be observed, due to Zeeman and Stark's effects. However, for the purpose of this thesis, no external field was considered, and calculations were only done for the maximum total angular momentum projection value, with a $2J + 1$ degeneracy taken into account in the following calculations.

$$1s^2 \; 2s^2 2p^5 \; 3s^2 \; 3p^6 \; 4s^1 \; 4p^1$$

$J = {}^1/_2$ $J = {}^3/_2$ $J = {}^5/_2$ $J = {}^7/_2$

$m_J = {}^{-1}/_2, \; {}^1/_2$ $m_J = \begin{matrix} -3/2, \; 3/2 \\ -1/2, \; 1/2 \end{matrix}$ $m_J = \begin{matrix} -5/2, \; 5/2 \\ -3/2, \; 3/2 \\ -1/2, \; 1/2 \end{matrix}$ $m_J = \begin{matrix} -7/2, \; 7/2 \\ -5/2, \; 5/2 \\ -3/2, \; 3/2 \\ -1/2, \; 1/2 \end{matrix}$

$\epsilon_{max=6}$ $\epsilon_{max=7}$ $\epsilon_{max=3}$ $\epsilon_{max=1}$

$6 + 7 + 3 + 1 = 17$ levels $6 \times 2 + 7 \times 4 + 3 \times 6 + 1 \times 8 = 66$ states
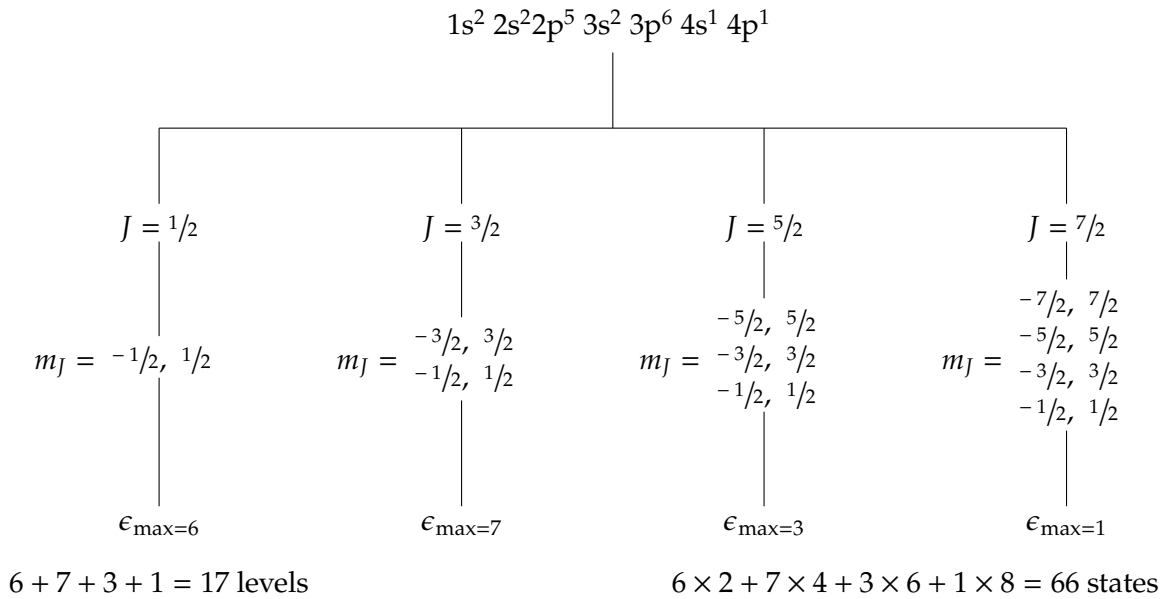
Figure 2.1: Splitting of quantum numbers for a given configuration.

In conclusion, an atomic level can be defined by the set of these three quantum numbers. In the notation used throughout this thesis, a level will be identified by:

$$i \equiv \left[(n\, l_j)_i;\, J_i;\, \epsilon_i \right], \tag{2.1}$$

And the energy of the level:

$$E_i \equiv E\left[(n\, l_j)_i;\, J_i;\, \epsilon_i \right], \tag{2.2}$$

2.3.2 Level calculation with *MCDFGME*

2.3.3 Level calculation with *MCDFGME*

For a given set of quantum numbers, a relativistic *MCDF* was performed using the *MCDFGME* script. The code executes an iterative self-consistent field calculation, accounting for both Coulomb and Breit's interactions, including the magnetic and retardation parts for the latter. For QED corrections, the formation of local potentials due to vacuum polarization was included in the self-consistent part of the calculation, while corrections due to self-energy were treated as perturbation. Furthermore, electron correlation was also accounted for by composing the antisymmetric wavefunction as a linear combination of state wavefunctions with mixing coefficients.

A typical level calculation begins with the formatting of the input `.f05` file. This file contains the necessary information and parameters the program needs for the computation that follows when the executable `mcdfgme2019.exe` is called. The input file has a certain structure in which certain calculation parameters are defined. A previously tailored template input file is used, where, by default, the previous contributions and the way they are accounted for in the numerical method are indicated. The template is then formatted in order to perform the calculation for the desired level. The element's atomic number and the electron configuration are selected with the former having the same format as in Annex I. The double of the value of the total angular momentum (as not to work with non-integer values) is included and so is the Lagrange multiplier/eigenvalue.

Other parameters, such as changing the initial trial wavefunctions and the parameters of the self-consistent calculation cycles can also be changed. Throughout the calculation these wavefunctions will go through a variational process, changing until the optimal solution is reached, as can be observed in Figure 2.2.

In order to reach optimal convergence, some of these parameters will need to be altered as to employ different numerical methods, but before these are discussed, it is necessary to provide an explanation as to how to evaluate the numerical convergence of the calculation:

> Olha lá se não tens que fazer o quadrado disso

2.3.3.1 Evaluating the convergence

After launching the `mcdfgme2019.exe` executable, the computation will start, generating an output file with the `.f06` extension, where the output will be written while the
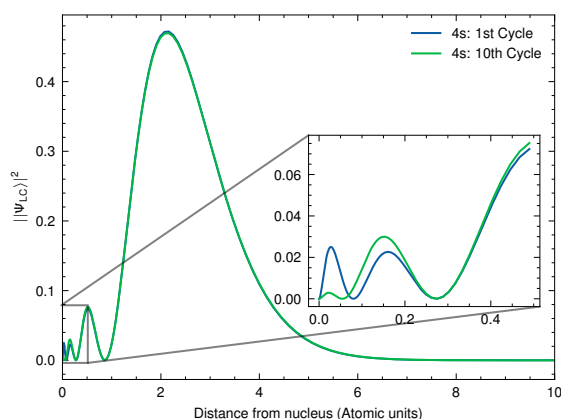
Figure 2.2: 4s Large component of the wavefunction after one and ten cycles of the self-consistent iterative process.

program is actively running.

One of the convergence benchmarks can already be evaluated while the calculation is being processed. Actively monitoring the output file with, as an example, the UNIX command `tail`, one can observe the output from the self-consistent cycles. Should the numerical method be diverging, warnings concerning sudden shifts in the wavefunction derivative may be displayed.

The calculation can also be aborted due to a numerical error. In this case, if the error occurred while running calculations for a certain orbital(s), this/these will be displayed in the output.

The three other parameters used when evaluating if the convergence was successful can be checked only after the calculation is over:

- Each cycle, a component of the level's energy is calculated through two different methods. These two values should be consulted for the last cycle and the absolute energy difference should be below a certain stipulated benchmark value (preferably lower than 1 eV).

- The wavefunction overlaps between each orbital sharing the same l_j value are displayed, since these cases are the most probable of having a convergence error leading them not to be orthogonal. The convergence is considered acceptable if every value is lower than 10^{-6}.

- For every orbital, the effective nuclear charge is calculated and displayed. This parameter is related to the shielding effect the charge of the electrons in other orbitals exert on the nuclear charge. If the calculation converged correctly, these values should never be equal to the extreme possible values: 0 or N, where N is the total number of electrons. For each orbital, this value should be close to an expected value .

Meter aqui ref de como calcular

2.3.3.2 Level convergence methods

First attempt at numerical convergence For the first calculation, by default, a simpler template file (Annex II) is used and a calculation of five self-consistent cycles is performed. All trial orbital wavefunctions are initialized by wavefunctions calculated using the Thomas Fermi potential [37].

Second attempt at numerical convergence Should the first attempt have failed to reach convergence, a similar calculation is performed, keeping the previous parameters, but increasing the number of self-consistent cycles to 10, enforcing for each, an increasingly more precise accuracy and higher number of iterations. The template can be found in Annex III.

Third attempt at numerical convergence Should the previous two attempts have been made, and no convergence was reached, a new calculation needs to be made. In addition to the change cycle parameters, the parameters for some orbitals are to be altered. This can be done by altering the initial wavefunction to hydrogenoid, or to a previously computed one. The method for solving the Dirac equation can also be changed for each chosen orbital. This final attempt can be quite time-consuming due to the many possibilities and combinations of methods to be employed for each orbital.

Since for every calculation thousands of levels need to be computed, a parallelized automation script was used. In total two scripts were used: a first one, previously written in `bash` by one of the advisors, Jorge Machado, which used GNU's `parallel` command [38] for parallelization, was used for the first calculations performed; and for most of the calculations, a new script, developed in the scope of this thesis, written in `Python` and employing an Message Passing Interface (*MPI*) approach for the purpose of parallelization. This last one will be discussed further in the thesis.

The total number of calculated 1-hole and 2-holes levels is displayed in Table 2.3.
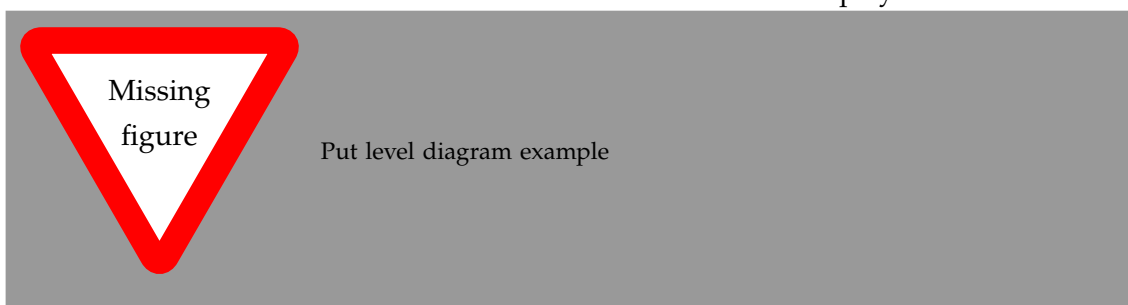
2.4 Transition computations

After all level computations have been performed, the next step towards the spectra simulation should be that of calculating level transitions. Any level that is not ground

Table 2.3: Total number of levels calculated. For all but the first row, the indicated orbital is the one where an electron was excited to.

Atomic System	Number of levels			Number of hand-converged levels		
	1-hole	2-holes	Total	1-hole	2-holes	Total
Cu^{1+}	19	183	202	0	1	1
4s	10					
4p	83	1001	1084	17	118	135
4d	107					
4f	114					
5s	33					
5p	83					
5d	107					
5f	114					
5g	115					
6s	33					
6p	83					
6d	107					
6f	114					
6g	115					
6h						
7p	83					
8p	83					
9p	83					
Total						

state will eventually decay into a more stable and less energetic one. This process is what eventually allows for the emission of x-ray radiation and Auger electrons.

When considering transitions between a given set of states, the transition energy and transition rate matrices are two 2D matrices of the greatest importance on spectra simulation, since their matrix elements contain the mentioned properties for all possible transitions across the set.

For an initial state denoted by i and a final one by f (using the notation from equation (2.1)), the matrix elements are as follows:

For the energy matrix:

$$E_{i,f} = E_i - E_f, \tag{2.3}$$

And now for the rate matrix:

$$R_{i,f} = R\left[(n, l_j)_i, J_i, \epsilon_i; (n, l_j)_f, J_f, \epsilon_f\right], \tag{2.4}$$

2.4.1 Diagram transitions

Diagram transitions are associated with radiative transitions between two 1-hole states. For ionized systems, this kind of transitions are associated to the characteristic radiation from principal spectral lines such as K_α, K_β, L, etc. For this reason, they are the focal point of study for the work performed on this thesis.

Given a set of all $n_{1-\text{hole}}$ 1-hole levels, one must consider only transitions from higher to lower energetic states. Therefore, the total number of diagram transitions, not taking account level degeneracy, N_{diag} can be simply calculated by the number of combinations of two 1-hole states:

$$N_{\text{diag}} = \frac{n_{1-\text{hole}}!}{2 \cdot (n_{1-\text{hole}} - 2)!},$$
(2.5)

For the rate calculation, the same approach was taken as in the works of Guerra [30] and Pinheiro [39], where the lack of orthogonality in the initial and final state due to numerical convergence is treated by the formalism present in Löwdin's work [40] and full orbital relaxation is allowed.

While *MCDFGME* calculates transition rates for both Coulomb (length) and Lorentz (velocity) gauges, only the length gauge calculated ones were used in this work. Rates are calculated for both Electric and Magnetic transitions and their many components (poles).

> needs to be checked

2.4.2 Auger transitions

As previous mentioned, these type of transitions are characterized by the transition's energy release coming in the form of an ejected electron, as opposed to x-ray radiation.

The set of initial and final states is now composed of the 1-hole and 2-hole sets. While for diagram transitions the total number of transitions could be calculated just by the number of elements in the set, in this case is not as simple, as the energy for every level has to be taken into account. The maximum number of possible transitions could be calculated by the product of the total number of 1-hole and 2-hole levels. The real number of transitions is, however, far away from this value.

Once again, the same procedure from [30, 39] was followed. Given the energy of the transition, the free electron wavefunction is calculated for the same potential as the initial state. This time, no relaxation is included, as to only account for the ionization, and orthogonality between the free wave and the bound orbitals is enforced.

2.4.3 Satellite transitions

This type of transitions are related to radiative relaxation between two 2-hole states. They are, therefore processed the same as Diagram transitions.

While they might not be of great relevance for this thesis, some were still calculated as they can be useful for other works due to being equivalent to some diagram transitions for Copper following shake-up.

The total number of calculated transitions can be found in Table 2.4:

Table 2.4: Total number of levels calculated. For all but the first row, the indicated orbital is the one where an electron was excited to.

Atomic System	Number of transitions			Total
	Diagram	Auger	Satellite	
Cu^{1+}	171	968	16653	
4s	45			
4p	3403			
4d	5671			
4f	6441			
5s	528			
5p	3403			
5d	5671			
5f	6441			
5g	6555			
6s	528			
6p	3403			
6d	5671			
6f	6441			
6g	6555			
6h				
7p	83			
8p	-			
9p	-			
Total				

2.4.3.1 Rate and Energy Matrices as a calculation quality evaluation tool

Due to *MCDFGME* applying a numerical method, even after employing the optimize orbital method for level calculation, the results obtained may not be accurate. This way a method for helping visualize the quality of a calculation is by plotting the rate matrix for the calculation.

The employment of this method was what lead to the decision not to perform the transition calculations for excitations to orbitals 8p and 9p, as well as excluding the results for excitation to 7p from the spectra simulation.

As an example, Figure 2.3 represents the rate matrix for 4p-excited Copper:

It is quite apparent that, as expected, only half the matrix elements are filled, due to transitions only occurring from higher to lower energy states. Moreover, transitions from np to 1s orbitals possessed the highest transition rate values, due to them composing the K spectrum, and the near-diagonal energy matrix elements present low energy values, due to being associated to similar state transitions. This city-like view is quite characteristic and can also be observed in all other successful calculations (consult Annex ??).
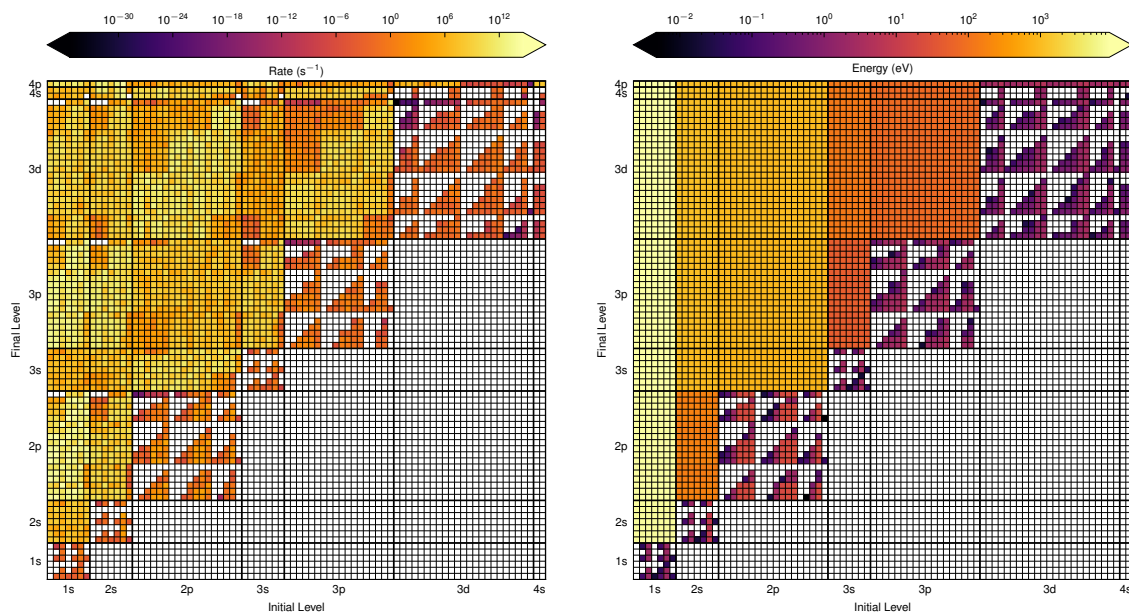
Figure 2.3: Rate Matrix for 4p-excited Copper.

In the case of 7p-excited Copper, the fact that the obtained result is not correct is quite apparent just by looking at Figure 2.4:
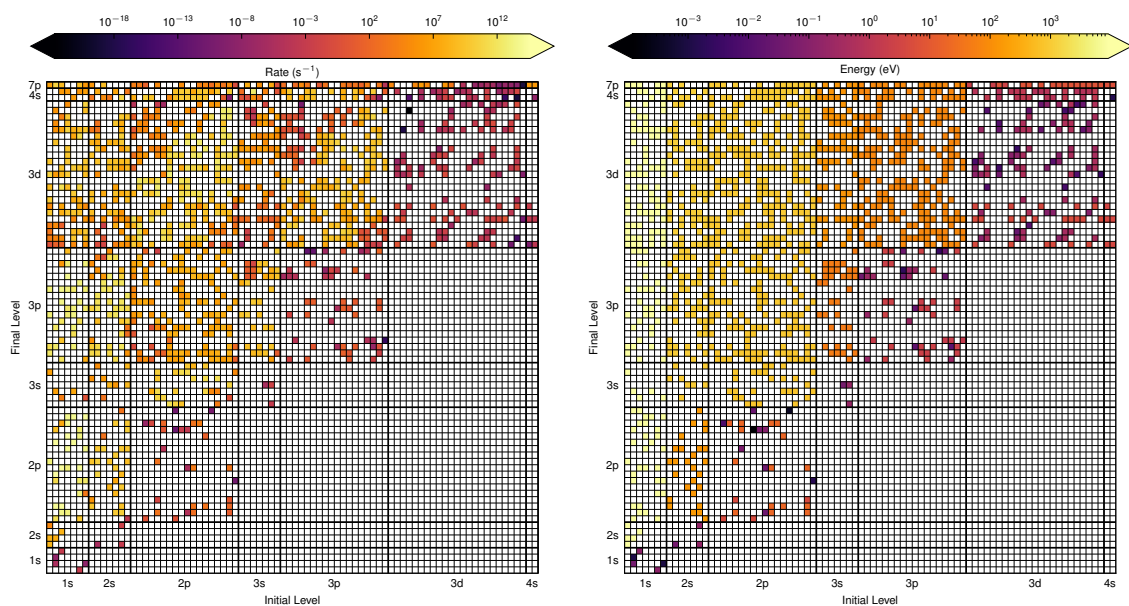

Figure 2.4: Rate Matrix for 7p-excited Copper.

Here, the fact that the upper electron is in such a high orbital could have lead to an improper convergence during the level calculation. This may be responsible for the wrong level energies, which in turn influenced the calculated transitions. Due to this behavior, no more transition calculations were performed for excitations to upper orbitals.

ver o que raios se passou com o 7p

25

Calculation of fundamental parameters

With every transition's energy and rate calculated, certain parameters of great relevance for spectra simulation, or even by their own merit can be now be computed.

3.1 Fluorescence Yield

alguma cena aqui

This parameter is, by itself, one of the most impactful. The Fluorescence Yield value for a given 1-hole state reflects the probability of said state to decay via radiative decay, as opposed to auger emission. In order to compute it, a few steps must be taken:

First, a reminder that, for each computed level i, due to its degeneracy, there is actually an amount of g_i states sharing the same properties:

$$g_i \equiv g\left[(n, l_j)_i, J_i, \epsilon_i\right] = 2J_i + 1, \tag{3.1}$$

That level's total radiative rate, R_i^R can now be computed as the sum of the rates for every transition from that level to another 1-hole level, denoted by f:

$$R_i^R = g_i \sum_f \cdot R_{i,f}^R, \tag{3.2}$$

The same procedure can be followed for the non-radiative rate, R_i^{NR} considering the final 2-hole levels:

$$R_i^R = g_i \sum_f \cdot R_{i,f}^{NR}, \tag{3.3}$$

That level's fluorescence yield, ω_i can now simply be calculated by:

$$\omega_i = \frac{R_i^R}{R_i^R + R_i^{NR}}, \tag{3.4}$$

This quantity, however, may not be of much relevance by itself. When discussing fluorescence yields, usually we are interested in the subshell's yield. In order to calculate

this value for the desired subshell, eg. K_1, the values for both rates should be summed for every level with a hole present in the subshell at study.

The values of the fluorescence yields for every calculated excited state can be found in Table 3.1:

Table 3.1: Fluorescence Yield for the first 9 subshells.

Atomic System	Fluorescence Yield								
	K_1	L_1	L_2	L_3	M_1	M_2	M_3	M_4	M_5
Cu^{1+}									
4s									
4p									
4d	3.483e-01	9.827e-04	8.647e-03		1.459e-05	4.479e-05		4.805e-09	
4f	4.469e-01	9.110e-04	9.055e-03		1.822e-05	5.073e-05		3.537e-07	
5s									
5p	4.297e-01	7.591e-04	1.829e-03		1.337e-05	3.877e-05			
5d									
5f									
5g									
6s									
6p									
6d									
6f									
6g									
6h									

3.1.1 Transition width

The full width of a level can only be calculated after all possible transitions have been computed. This width arises due to the fact the level can decay into others with a certain rate and is associated with the natural broadening give by Heisenberg's uncertainty principle ($\Delta E \Delta t \geq \hbar$). The width of the level, Γ_i, is given by:

$$\Gamma_i = \hbar \cdot \left(R_i^R + R_i^{NR} \right), \tag{3.5}$$

Now, for the calculation of the full width of an atomic transition, $\Gamma_{i,f}$, the level for both initial and final states is considered:

$$\Gamma_{i,f} = \Gamma_i + \Gamma_f, \tag{3.6}$$

3.2 Transition intensity

The final parameter needed for a preliminary spectra simulation is the intensity of the transition.

27

For the calculation of this parameter, one must look not only at the transition's rate, but also at the weight of the initial level in the whole set that share a hole in the same subshell. For this, the subshell's multiplicity needs to be computed:

$$g_{sub} \equiv g\left[(n, l_j)_i\right] = \sum_{J, \epsilon} g\left[(n, l_j)_i, J, \epsilon\right], \tag{3.7}$$

The level intensity can now be computed as proportional to the product of the statistical weight of the level with the branching ratio of the transition, and the level's fluorescence yield:

$$I_{i,f} \equiv I\left[(n, l_j)_i, J_i, \epsilon_i; (n, l_j)_f, J_f, \epsilon_f\right] = N_i \underbrace{\frac{g_i}{g_{sub}}}_{\text{Statistical weight}} \underbrace{\frac{R_{i,f}}{R_i^R}}_{\text{Branching ratio}} \omega_i, \tag{3.8}$$

Which can be further simplified:

$$I_{i,f} = N_i \frac{g_i}{g_{sub}} \frac{R_{i,f}}{R_i^R} \frac{R_i^R}{R_i^R + R_i^{NR}} = N_i \frac{g_i}{g_{sub}} \frac{R_{i,f}}{R_i^R + R_i^{NR}}, \tag{3.9}$$

In equations (3.8) and (3.9), N_i works as a scaling parameter to account for the density of atomic systems that are found in the state i. In the case of an ionized system, when comparing emissions generated due to a hole in the same subshell, the probability of generating that hole is approximated as being the same for all relevant levels, and this value is typically attributed a value of 1. A spectrum simulated using this consideration can be further found in Figure 4.1. This approximation, however is not valid when dealing with resonant photoexcitations, as will be discussed in the next section.

Spectra simulation

This chapter is the culmination of all the work performed on this thesis. Synthetic theoretical spectra will be computed using the calculated parameters from chapters 2 and 3. For the simulation of the resonant effect, a new approximate method for estimating photoexcitation cross-sections will be developed.

4.1 Theoretical line shapes

Even though an atomic state transitions possess well-defined energy values, as calculated in chapter 2, it is now also clear that these transitions also have an energetic uncertainty to them, given by the sum of the energy widths of the initial and final levels (equation (3.6)). The theoretical emission shape is given by a Lorentzian profile, centered around the emission energy, $E_{i,f}$, with a FWHM of $\Gamma_{i,f}$ and an amplitude of $I_{i,f}$:

$$L \equiv L\big(E - E_{i,f}, \Gamma_{i,f}, I_{i,f}\big) = \frac{I_{i,f}}{2\pi} \frac{\Gamma_{i,f}}{\big(E - E_{i,f}\big)^2 + \big(\Gamma_{i,f}/2\big)^2}, \tag{4.1}$$

This profile, however, would only be valid for the emission of radiation by stationary atoms (with no thermal distribution) and does not account for the detection of said radiation and interactions it may have with the experimental apparatus, with these last considerations being nondeterministic, but stochastic in nature. To account for this, a new broadening should be considered.

A common way to tackle this problem is to compute the convolution of the theoretical shape from equation (4.1) with the Gaussian profile from equation (4.2).

$$G \equiv G(E, \sigma) = \frac{1}{\sigma\sqrt{2\pi}} \exp\left(-\frac{E^2}{2\sigma^2}\right), \tag{4.2}$$

The σ parameter should account for Doppler shifts caused by thermal distributions, stochastic effects in the experimental setup and the radiation detection system's resolution. This operation results in a specific type of profile also known as Voigt:

$$V \equiv V\left(E - E_{i,f}, \Gamma_{i,f}, \sigma, I_{i,f}\right) = \int_{-\infty}^{\infty} L \cdot G \, \mathrm{d}E \,, \tag{4.3}$$

Due to the complexity of the convolution operation, there is no simple analytical expression for obtaining values from the Voigt distribution. They can, however, be computed by taking the Real part of the Faddeeva function, $w(z)$:

$$V(z) = \frac{\mathrm{Re}\{w(z)\}}{\sigma\sqrt{2\pi}}, \quad z = \frac{E - E_{i,f} + i\Gamma_{i,f}}{\sigma\sqrt{2}}, \tag{4.4}$$

In Figure 4.1, the theoretical K_α spectrum for ionized Copper, using the $N_i = 1$ approximation, previously mentioned in section 3.2, is displayed for both when only accounting for emission, and for when considering an experimental resolution of 2 eV.
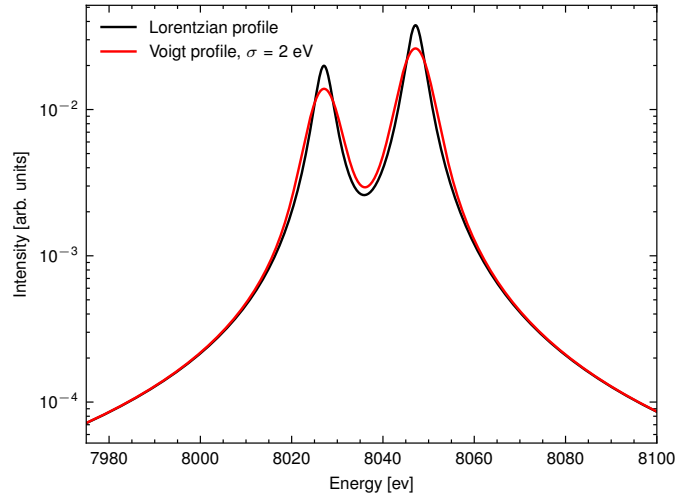
Figure 4.1: Comparison of a Lorentzian and Voigt profile for Copper's characteristic K_α transitions. The red line is the obtained result after convolution the black line with a $\sigma = 2$ eV Gaussian profile.

4.2 Computing the photoexcitation effect

The final step needed in order to simulate the theoretical spectra is that of calculating the scaling factor N_i as a function of the energy of the incident beam.

4.2.1 The beam profile

The objective for this thesis is that of simulating the effect an x-ray beam coming from a synchrotron line with energies close to that of Copper's K-shell ionization threshold has on the measured x-ray emission spectrum. The incident synchrotron radiation, through the usage of wigglers and undulators can reach a near monochromatic distribution, with energy spreads on the scale of only a few hundred meV.

From this point forward, a Gaussian profile will be considered for the incident beam. This profile has a tunable energy, in order to survey the whole near-ionization threshold region, and a broadening parameter $\sigma = 0.5$ eV.

4.2.2 Simulating the resonance

It is now necessary to calculate the N_i parameter as to account for both the beam profile and the resonance. For an accurate spectra simulation, this value should be that of the photoexcitation cross-section. This, however, is simply not easy to calculate. While *MCDFGME* is able to calculate photionization cross-sections, it is not for the photoexcitation case. Experimental data was also not found, but that would go against the *ab-initio* objective of this thesis. A good approach would be to perform R-Matrix calculations , but due to their complexity, it was not possible to achieve this at this stage.

In order to solve this problem, assumptions had to be made. First, steady state was assumed, as well that every Cu atom could only be found in ground state before beam-interaction. Second, for every given transition, three states were assumed: the initial ground state, the intermediate excited state, and the final post-relaxation state.

In order to estimate a scaling factor for the population of the intermediate state, it was assumed that, for a given beam energy distribution, the rate of excitation from the ground state to the excited state would be proportional to that of the direct decay from the excited to ground state, since the mediation interaction is the same for both of them, only on an inverse order. Both processes occur with a photon absorbed/emitted from the system and an electron changing orbital.

Since for the purpose of state population only the decay from the excited state to the ground state was accounted for, the full width of the transition is only composed by that single partial width, since there is only one decay channel. In order to compute the parameter N_i, the overlap of the beam profile and a Lorentzian profile with width equal to that of the transition and with an amplitude equal to the rate was taken:

$$N_i = R_{exc} \int_{-\infty}^{\infty} G(E - E_{beam}, 0.5 \text{ eV}) \cdot L(E - E_{exc}, \Gamma_{exc}) \, \mathrm{d}E \, , \qquad (4.5)$$

This way it is ensured the resonance peak occurs at the excitation energy and takes into account the beam energetic distribution.

Taking into account every calculated excited state, Figure 4.2 contains every Lorentzian contribution. This resonant spectrum could be somewhat proportional to the excitation component of Copper's absorption spectrum.

From Figure 4.2, there is something quite notorious. While for most excited states, the absorption energies related to K-shell excitation can be found close together, in the case of the excitation to orbital $4p$, two levels converged to an energy value diverging from the others by around 3 eV. While this could have arisen from a numerical convergence problem, all convergence parameters were confirmed and other more complex methods employed,
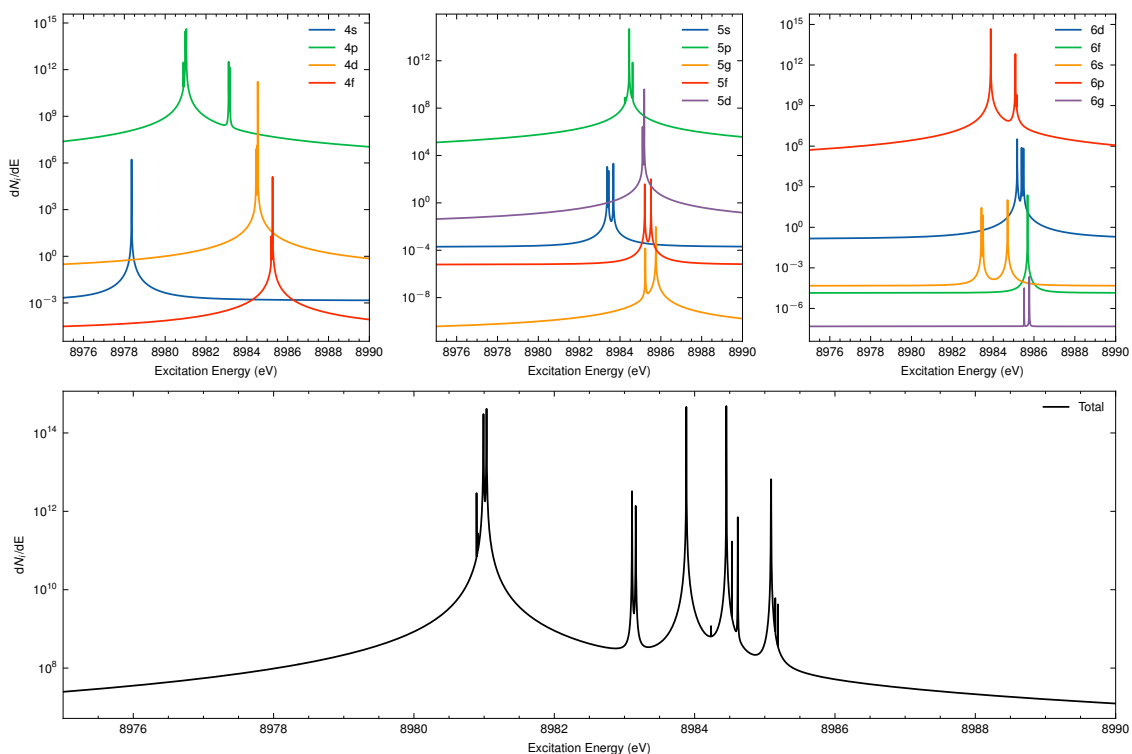
Figure 4.2: Differential scaling parameter accounting for every excitation contribution. The legend indicates the orbital the electron was excited to.

with no change in the level energy. This energy difference will have a great impact in the simulated spectrum, since this excitation is the one with the highest probability.

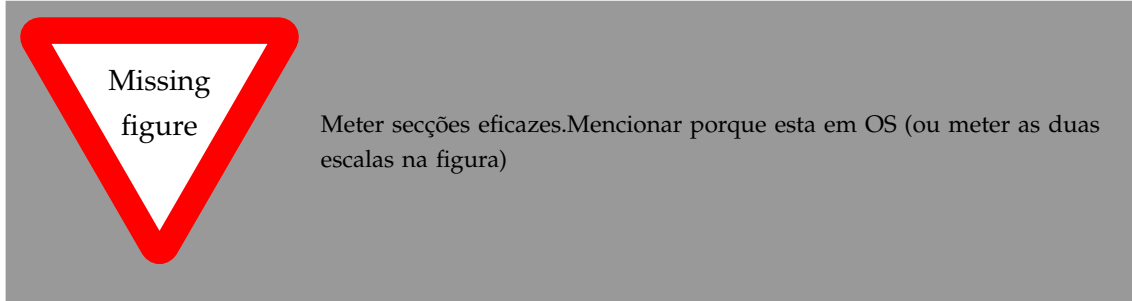## 4.3 Computing the photoionization effect

It is now necessary to account for the effects that ionized Copper has on the spectrum, all while finding a way to calculate N_i that is also compatible with the photoexcited case.

Assuming ground state Copper as a starting point, following the ionization of the K shell, two levels are possible: one where the 1s and the 4s electron's spins counter-align, resulting in a J value of 0 and multiplicity 1, and one where they align, resulting in $J = 1$ and a multiplicity of 3. The ionization energy can be calculated for both level possibilities by the energetic difference between the levels, resulting in a theoretical value of 8986.02502 eV for the singlet and 8985.93363 eV. It should be noted that the theoretical values are shifted by more than 5 eV from most values present for solid-state Copper in the standard x-ray databases, such as xraylib's of 8978.9 eV [41], and NIST's 8980.476(20) eV [42]. It is, however, quite similar to the K-edge values for Vaporized Copper, also present in NIST's database 8987.89(50) eV [42]. This shift is due to solid-state interactions between the Copper atoms displaying crystalline patterns resulting in a decrease in the binding energy.

The photoionization cross-sections were obtained using the *MCDFGME* code, with the same settings of orthogonality enforcing and no relaxation allowed used for auger

transitions for energies from the ionization threshold up to ????. Figure ?? displays the `[insert later]` obtained results. An independent *MPI* script was developed for faster calculations for a large set of photon energies.

Missing figure

Meter secções eficazes.Mencionar porque esta em OS (ou meter as duas escalas na figura)

From the zoom-in view on the previous figure, it is apparent that the cross-section are not accurate for near-ionization energies, as can be seen by the slow rise and oscillatory behaviors. This is an artifact of the calculation method and these values do not display the true nature of the photoionization effect. In order to properly estimate them, a 3-exponential fit was performed for both curves, for higher energies (10 keV), and values were extrapolated for the near-ionization threshold, with a sudden drop to 0 for values lower than the theoretical ionization energy. `[meter aqui valores]`

While it was possible to calculate the proper cross-section values, the N_i parameter needed compatibility to the way it was computed in the photoexcited state, so the correlation between the Oscillator Strength and Rate needed was needed.

On the case of radiative transitions, for the electric components, besides yielding the rate value, *MCDFGME* also outputs the correspondent value for the Oscillator Strength. A proportionality was found between these two parameters, the emitted photon energy, and the ratio between the initial and final state multiplicities. `[meter a equação]`

It is now possible to convert the photoionization cross-sections into something that is rate normalized so that the overlap can be calculated with the beam profile and the parameter N_i computed. In a similar but inverse fashion, the photoexcitation cross-sections, can be calculated and are present in Annex ??.

4.4 The synthetic spectrum

The energy of the beam profile used for simulation was tuned as to survey the whole pre-excitation region up to post K-shell ionization. From an initial beam energy of 8970 eV up to a final of 8995 eV, in steps of 0.01 eV, the spectra were simulated taking into account the whole set of contributions. As expected, for the excitations, the diagram transitions for 4p-excited Copper have the greatest impact on the spectrum. This is due to it being the $ns \rightarrow n'p$ excitation to the lowest possible n' value. These are followed by other `[Justifica melhor isto]` $n'p$-excited states, with the spectral intensity decreasing by an order of magnitude for each consequent n'. The spectral 2D plots, containing the x-ray emissions as a function of beam energy for each component can be found in Annex ??, while the full spectrum is present

in Figure 4.3. Due to the previously mentioned energy divergence for some $4p$ excited levels, two distinct resonant areas will appear on the spectrum for this contribution.
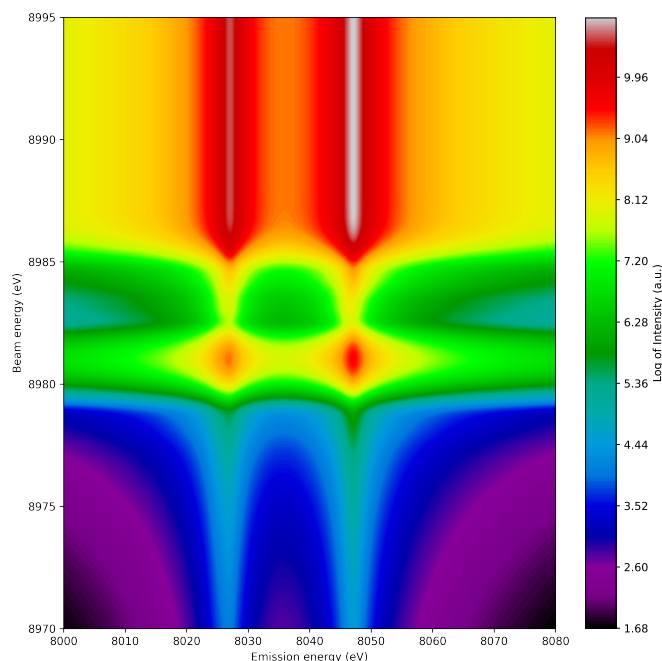

Figure 4.3: Copper's x-ray emission spectrum as a function of beam energy.

From this view, it is quite obvious the presence of three high-intensity regions. Both lower energy ones are $4p$-excitation dominated, while the high energy one, where a clear plateau region is observed is due to the photoionization. As expected, this last component would be the dominant one once the threshold has been reached. In the next chapter, the effect other excited states have on the emission energy will be further explored, as to be more apparent.

As previously mentioned, some numerical convergence problems may have occurred for the calculation of excitations to np orbitals. This is apparent when looking at the plots with the isolated contributions from $4p$ and $6p$ excited orbitals, where some "tails" can be observed near the main resonance.

Spectral analysis

Now that the theoretical spectrum has been simulated, it is time to analyze the evolution of the emission lines with the change in the beam energy. Results will then be compared with a recent work by Y. Ito ?? where measurements of Copper's x-ray transitions were taken for

5.1 Result analysis

For the purpose of peak analysis of the K_α spectrum, it is common practice to employ either four Lorentzian profile, or two asymmetrical ones. The latter approach was the one applied for this study.

In order to compute the asymmetrical Lorentzian profile, an asymmetry parameter, α, was incorporated:

$$L_{\text{assim}}(E - E_{i,f}, \Gamma_{i,f}, \sigma, \alpha) = \frac{I_{i,f}}{2\pi} \frac{\Gamma_{i,f}}{\left(\frac{E - E_{i_f}}{\alpha \cdot \text{sign}\left(E - E_{i_f}\right) + 1}\right)^2 + \left(\frac{\Gamma_{i,f}}{2}\right)^2} \tag{5.1}$$

The influence of the calculated excitations, namely to orbital $5p$, will now be noticed in the evolution of the parameters, resulting, in some cases, in extremely non-linear parameter progression.

5.1.1 Centroid energy

For the K_{α_1} line, a very noticeable energy shift of around 0.5 eV is observed at the second $4p$ resonance-dominated zone. Once again, poor numerical convergence may be the cause of this.

On the case of the K_{α_2} line, the results are less anomalous, as there is a steady rise of the centroid energy, with the influence of different excited states being noted as sudden bumps and lows.

Both spectral line energies are lower on the pre-ionization region, and saturate for beam energy values over the K edge, with K_{α_1} possessing an energy of (8047.093 ± 0.002) eV and K_{α_2} of (8026.683 ± 0.004) eV at $E_{\text{beam}} = 8970$ eV, and rising to (8047.12926 ± 0.00001) eV and (8027.05247 ± 0.00002) eV, respectively, for the post-ionization region.

Figure 5.1 contains the whole evolution of the centroid parameters as well as indications for the major excitation contributions.
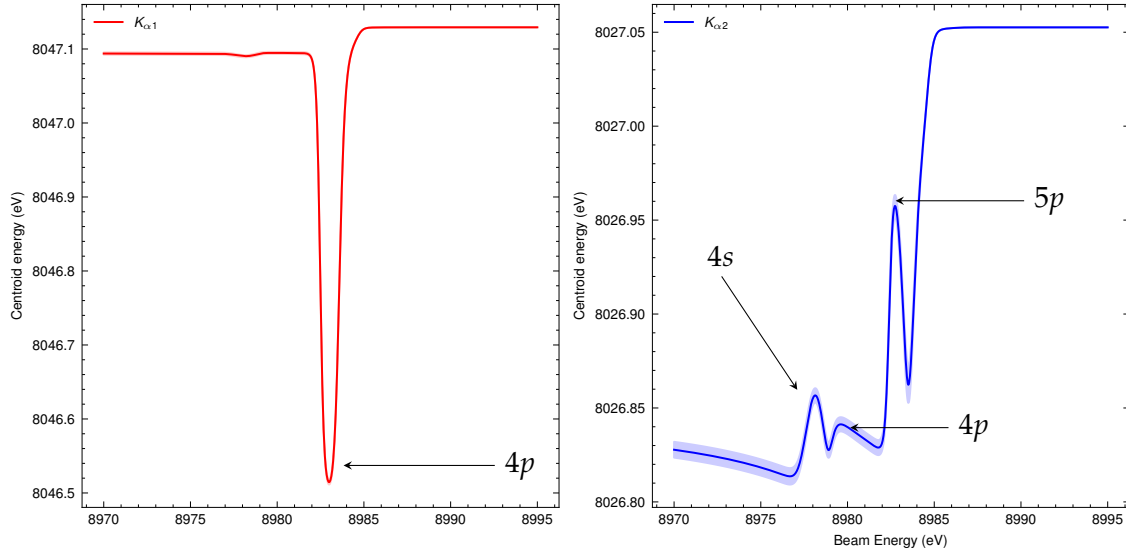
Figure 5.1: Evolution of centroid parameter as a function of the beam energy. The bands colored bands include the parameter fitting errors.

5.1.2 Energy width

Both K_α transitions present an energy width value of around 2.2 eV for the post-ionization region $((2.25137 \pm 0.00003)$ eV and (2.21834 ± 0.00006) eV for K_{α_1} and K_{α_2}, respectively). Both present higher values than these for the excitation-dominated region, with K_{α_2} being wider than K_{α_1}.

The fact the transition widths for the photoexcitation region present a higher value than for the standard K_α transitions for ionized Copper could be easily explained by the increase in the amount of Auger decay channels due to the presence of a lesser bound electron, whose transitions will lead to greater level widths.

5.1.3 Spectral intensity

The main takeaway point from this parameter is the growth is the immense evolution of the spectral intensity. From the lowest simulated beam energy to the post-ionization regime, the spectral intensity for both lines grows by 6 orders of magnitude. Only decays from $4p$ excited levels seem to influence significatively the spectral intensity, as can be noticed by the increase in intensity on Figure ??.
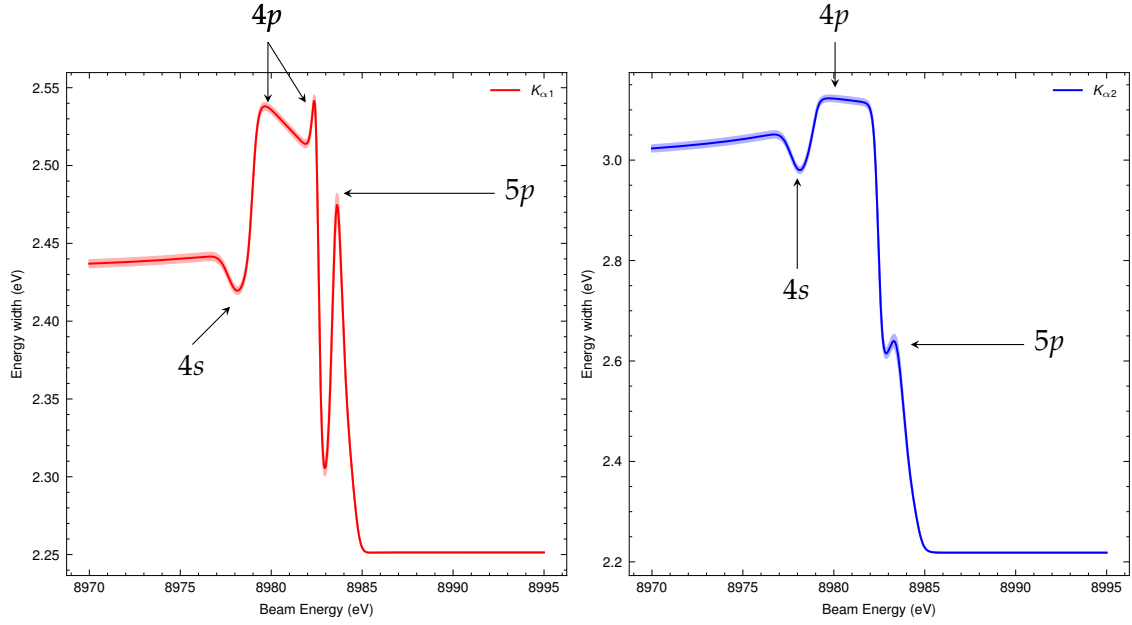
Figure 5.2: Evolution of transition width as a function of the beam energy.
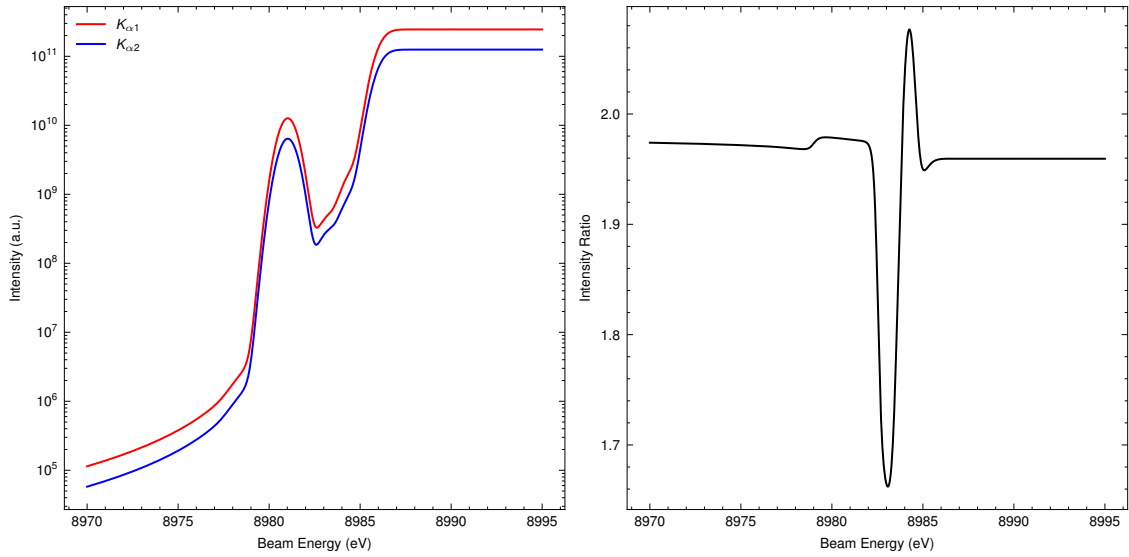

Figure 5.3: Evolution of the spectral intensity and intensity ratio.

In addition, from the same figure, it can also be concluded that the ratio between K_{α_1} and K_{α_2} intensities, while it is about the same for most of the surveyed energies, it rapidly oscillates near the $5p$ and higher excitation energy resonances, stabilizing once again for higher energies, where ionization predominates.

5.1.4 Asymmetry index

For the model used, a negative value for the asymmetry index indicates a skewness to lower energies, while a positive for higher energies.
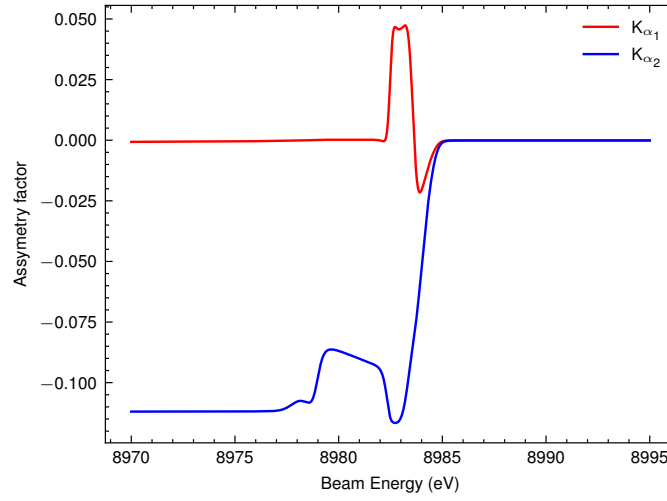
Figure 5.4: Evolution of asymmetry index.

Figure 5.4 shows the evolution of this parameter for both spectral lines. While the K_{α_2} presents a constant left-skewness up until the ionization region, K_{α_1} presents as symmetric up until the second $4p$ excitation area, where it acquires a positive skewness factor, which consecutively drops when entering the area where the $5p$ excitation dominates. Both lines go back turn symmetric ($\alpha = 0$) when the ionization region is reached.

5.2 Comparison with experimental results

It is unfortunate that not many of experiments have been run for exploring the phenomenon of photoexcitations of K-shell electrons and the consequent decays. Due to the low spectral intensity, and the fine structure of the resonances, exploring the photoexcitation effect can be quite challenging.

In a recent work by Y. Ito , near-threshold beam energies produced in a synchrotron line have been used to probe a Copper target. The consequent emitted radiation was then measured by the means of a Double Crystal Spectrometer. The wavelength dispersive nature of this apparatus allows for very precise filtering of the measured energy, allowing for experimental resolutions lower than 1 eV. The beam energy was tuned from values as low as 8978 eV, which falls under the theoretical excitation-dominated region, up to post-ionization threshold values. In this experimental setup, however, the measured K-edge presented a value of 8980.06 eV, so only a small portion of the measured spectrum can be of interest.

The K_α lines were consequently measured and fitted with Lorentzian profiles. Figure ?? shows the parameter evolution of the measured spectrum.

The main takeaway points for comparison between the calculated theoretical spectrum and the measured experimental one, is that both present larger widths for bellow-ionization threshold energies.
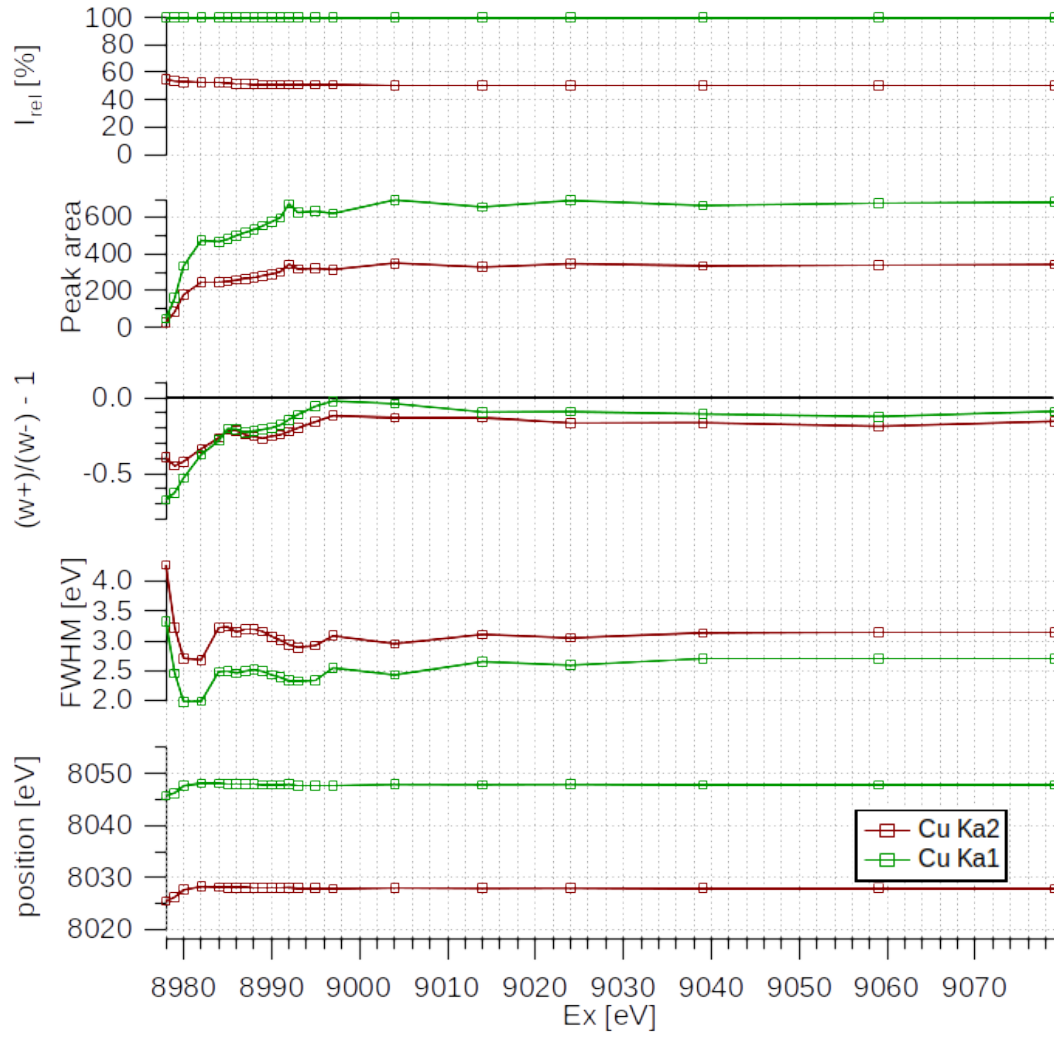
Figure 5.5: Components of the Lorentzian profiles employed in the fitting of the K_α spectrum. From ??.

On the emission spectrum, measurements have been performed for near K-edge beam energies.

A new High-Performance Computing code for parallelization of atomic structure calculations

As previously discussed, when dealing with an atomic structure calculation, the branching-out of the levels lead to the necessity to perform thousands of computations both for level and transition calculations. In order to aid in this process, and to perform the necessary calculations in a reasonable time, parallelization scripts are used. The subject of this chapter will be the developed python *MPI* implementation. The full `runMCDF_MPI.py` code with proper documentation can be found in .

link

6.1 An overview

The developing of this script was motivated by a few key points. The main one is due to the fact that scripts employing *MPI* can easily be wrapped by `SLURM` and be used in a supercomputer with a cluster architecture. The second motivation is due to the previously utilized script (written in `bash` by one of the advisors and employing the `parallel` command) not being able to perform calculations for some desired excitations, and, at last, `python` being a much suitable language for adding new features.

The working principle for this script is the deployment of numerous Slave ranks (limited by the number of the CPU hardware threads) which perform the computations in a parallelized way, and communicate with a Master rank which has only the function of managing the slaves' workloads, and compiling the obtained results.

In its current state, the code encompasses many features, such as:

- Level calculation for a given set of 1 and 2-holes configurations.

- Radiative, Auger and Satellite transition rate calculations.

- Spectral intensity calculations

- Interface for level convergence with active output control.

- Spawning of a terminal per rank for debugging purposes.

A very brief explanation on the working principle of each calculation follows.

6.1.1 Level calculation

The level calculation is started first by a quantum-number finding process, and then followed by the actual calculations.

For initially finding the whole set of levels, the user-defined configurations are loaded into the master rank's work queue. These are then distributed to rank slaves who will try to execute an *MCDFGME* calculation for an extremely high J value. An error output will indicate the maximum possible J value, which the slave rank will communicate to the master, who will, in turn, spawn calculations for all possible J values.

For finding all possible eigenvalues, a similar process is followed, where a trial calculation, now with the correct J value, is ran for a high eigenvalue, in order to let the *MCDFGME* find the maximum possible value. Taking this into account, the master rank is able to spawn proper calculations for the whole set of levels.

For each level, the three convergence attempts will be performed. Should all of them fail, the level is sent for manual converged.

6.1.2 Transition calculation

The first step in order to compute all possible transitions is to order the calculated levels by their energy. For each individual level a transition calculation will be performed for all less energetic levels. This involves using the wavefunction-containing `.f09` files for both initial and final levels.

Should the transition involve two 1-hole or two 2-hole levels, a radiative transition is calculated, while for a set of 1-hole and 2-hole levels, an auger transition calculation is performed.

This operation is the one that takes the most computational time, due to high number of transitions.

6.1.3 Spectral intensity calculations

The process for the calculation of these parameters follows the definitions presented in section??. This process is the only non-paralleized calculation performed by the script, as the master slave is able to compute every intensity in a matter of only a few seconds.

In order to aid calculations, the data analysis library `pandas` [43] was used, leading to a major improvement in computational time when compared to the previously used `bash` script.

6.1.4 Level convergence interface

The manual level convergence process is by itself, quite tiresome. It involves changing directory multiple times, launching and exiting text editors every time an attempt is made, as well as manually checking for the convergence parameters. The time and energy lost in this process can be quite significant for longer calculations.

In order to mitigate this, a state convergence interface was created. When launching this interface, the user is able to select the desired energy difference and overlap values for convergence benchmarking, and, by itself, the interface will cycle through all calculated levels, stopping when the stipulated conditions are not met.

In this case, the quantum numbers are displayed, as well as the level energy, energy difference, and maximum overlap values on the left side of the screen, while on the right the `.f06` output is displayed. With a simple press of a button, the user can either open the input `.f05` file on a `nano` text editor, run a *MCDFGME* calculation, or skip to the next failed level, should the previous one be up to standards.

The use of this interface greatly accelerated part of the work performed on this thesis.

Missing figure

meter print da interface.
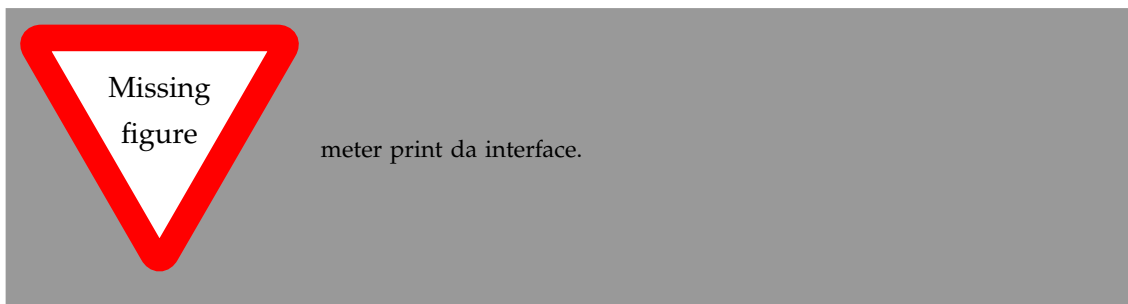
6.2 Speedup comparison

When dealing with code parallelization, one of the most important features is the evolution of the execution time as a function of the number of working ranks.

Due to the numerical nature of the calculations performed by `mcdfgme2019.exe`, the time taken to perform a computation varies a lot based on the system at study and methods employed. This way, a more demanding calculation, even when only being executed by a single rank, can impact the whole performance of the system, affecting other ranks.

In order to evaluate and compare the parallelization capability of the developed script, the same computation was performed using the current and the previous script, for a variable number of working ranks.

Missing figure

Comparar scripts e Amhdal
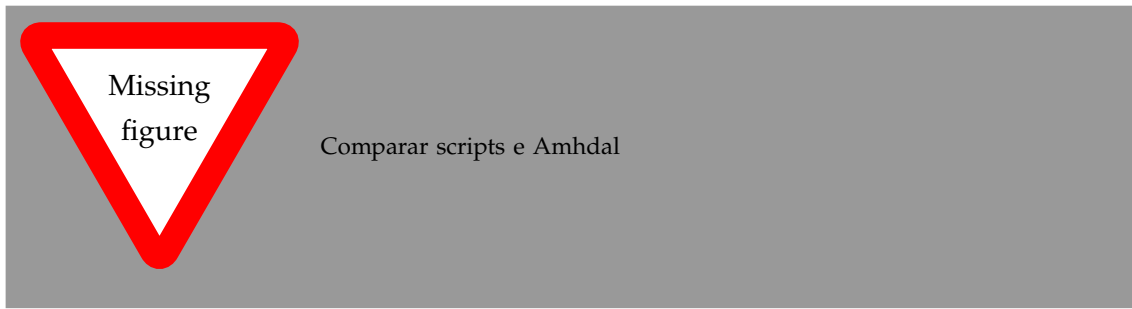
6.3 Advantages and Disadvantages

6.4 Future improvements

Bibliography

[1] T. D. Thomas. "Transition from Adiabatic to Sudden Excitation of Core Electrons". In: *Phys. Rev. Lett.* 52 (6 1984), pp. 417–420. DOI: `10.1103/PhysRevLett.52.417`. URL: `https://link.aps.org/doi/10.1103/PhysRevLett.52.417` (cit. on p. 5).

[2] M. F. Vitha, R. Klockenkämper, and A. V. Bohlen. *Chemical Analysis: A Series of Monographs on Analytical Chemistry and Its Applications Total-Relection X-ray Fluorescence Analysis and Related Methods*. 2nd Edition. Vol. 181. 2015, pp. 20–21 (cit. on pp. 6, 51).

[3] *Hartree Fock method: A simple explanation*. URL: `https://insilicosci.com/hartree-fock-method-a-simple-explanation/` (cit. on p. 8).

[4] J. P. Santos. *FÍSICA ATÓMICA Apontamentos para a UC FA 2020/21* (cit. on p. 8).

[5] R. Gabriel and T. Rosa. *The Hartree-Fock Method* (cit. on p. 8).

[6] S. M. Blinder. *Introduction to the hartree-fock method*. 2018-01. DOI: `10.1016/B978-0-12-813651-5.00001-2` (cit. on p. 8).

[7] B. Thaller. *The Dirac Equation*. Springer Berlin Heidelberg, 1992. DOI: `10.1007/978-3-662-02753-0` (cit. on p. 9).

[8] H. F. Beyer and V. P. Shevelko. *Introduction to the physics of highly charged ions*. IOP Pub, 2016, pp. 1–361. ISBN: 9781420034097. DOI: `10.1016/s0168-9002(03)00733-2` (cit. on p. 9).

[9] J. J. Sakurai and J. Napolitano. *Modern Quantum Mechanics*. Cambridge University Press, 2020-09. DOI: `10.1017/9781108587280` (cit. on p. 9).

[10] H. A. Bethe and E. E. Salpeter. *Quantum Mechanics of One- and Two-Electron Atoms*. Springer US, 1977. DOI: `10.1007/978-1-4613-4104-8` (cit. on pp. 9, 12).

[11] M. Strickland. *Relativistic Quantum Field Theory, Volume 1*. 2053-2571. Morgan & Claypool Publishers, 2019. ISBN: 978-1-64327-702-8. DOI: `10.1088/2053-2571/ab30cc`. URL: `https://dx.doi.org/10.1088/2053-2571/ab30cc` (cit. on p. 10).

[12] P. A. M. Dirac. "The quantum theory of the electron". In: *Proceedings of the Royal Society of London. Series A, Containing Papers of a Mathematical and Physical Character* 117 (778 1928-02), pp. 610–624. ISSN: 0950-1207. DOI: `10.1098/rspa.1928.0023` (cit. on p. 10).

[13] D. Bank. *Atomic physics at GSI / FAIR:current and future research.* 2023-08 (cit. on p. 13).

[14] T. V. Nguyen et al. "Theory of copper K_α and K_β diagram lines, satellite spectra, and ab initio determination of single and double shake probabilities". In: *Physics Letters, Section A: General, Atomic and Solid State Physics* 426 (2022-02), p. 127900. ISSN: 03759601. DOI: `10.1016/j.physleta.2021.127900`. URL: `https://linkinghub.elsevier.com/retrieve/pii/S0375960121007659` (cit. on p. 14).

[15] H. A. Melia et al. "The characteristic radiation of copper K_β including radiative Auger processes". In: *Journal of Physics B: Atomic, Molecular and Optical Physics* 53 (19 2020-10), p. 195002. ISSN: 13616455. DOI: `10.1088/1361-6455/aba3a6`. URL: `https://iopscience.iop.org/article/10.1088/1361-6455/aba3a6` (cit. on p. 14).

[16] H. A. Melia et al. "The characteristic radiation of copper K_α 1,2,3,4". In: *Acta Crystallographica Section A: Foundations and Advances* 75 (3 2019-05), pp. 527–540. ISSN: 20532733. DOI: `10.1107/S205327331900130X`. URL: `http://www.ncbi.nlm.nih.gov/pubmed/31041908` (cit. on p. 14).

[17] H. Sorum. "The K_α1,2 X-ray spectra of the 3d transition metals Cr, Fe, Co, Ni and Cu". In: *Journal of Physics F: Metal Physics* 17 (2 1987-02), pp. 417–425. ISSN: 03054608. DOI: `10.1088/0305-4608/17/2/011` (cit. on p. 14).

[18] J. Bremer, T. Johnsen, and H. Sørum. "The Cu K_α1,2 spectrum as measured with a curved-crystal spectrometer". In: *X-Ray Spectrometry* 11 (3 1982), pp. 149–152. ISSN: 10974539. DOI: `10.1002/xrs.1300110312` (cit. on p. 14).

[19] M. Deutsch et al. "K and K x-ray emission spectra of copper". In: *Physical Review A* 51 (1 1995-01), pp. 283–296. ISSN: 10502947. DOI: `10.1103/PhysRevA.51.283` (cit. on p. 14).

[20] Y. Ito et al. "K_α1,2 x-ray linewidths, asymmetry indices, and [KM] shake probabilities in elements Ca to Ge and comparison with theory for Ca, Ti, and Ge". In: *Physical Review A* 94 (4 2016-10), p. 042506. ISSN: 24699934. DOI: `10.1103/PhysRevA.94.042506` (cit. on p. 14).

[21] H. Berger. "Study of the K_α emission spectrum of copper". In: *X-Ray Spectrometry* 15 (4 1986-10), pp. 241–243. ISSN: 0049-8246. DOI: `10.1002/xrs.1300150405`. URL: `https://onlinelibrary.wiley.com/doi/10.1002/xrs.1300150405` (cit. on p. 14).

[22] S. Galambosi et al. "Near-threshold multielectronic effects in the Cu $K_{\alpha_{1,2}}$ x-ray spectrum". In: *Physical Review A - Atomic, Molecular, and Optical Physics* 67 (2 2003-02), p. 5. ISSN: 10941622. DOI: 10.1103/PhysRevA.67.022510. URL: https://link.aps.org/doi/10.1103/PhysRevA.67.022510 (cit. on p. 14).

[23] C. T. Chantler, A. C. Hayward, and I. P. Grant. "Theoretical Determination of Characteristic X-Ray Lines and the Copper K_α Spectrum". In: *Physical Review Letters* 103 (12 2009-09), p. 123002. ISSN: 00319007. DOI: 10.1103/PhysRevLett.103.1230 02. URL: https://journals.aps.org/prl/abstract/10.1103/PhysRevLett.103 .123002 (cit. on p. 14).

[24] F. Gel'mukhanov and H. Ågren. *Resonant X-ray Raman scattering*. Vol. 312. Elsevier, 1999, pp. 87–330. DOI: 10.1016/S0370-1573(99)00003-4 (cit. on p. 14).

[25] P. Carra, M. Fabrizio, and B. T. Thole. "High resolution x-ray resonant Raman scattering". In: *Physical Review Letters* 74 (18 1995-05), pp. 3700–3703. ISSN: 00319007. DOI: 10.1103/PhysRevLett.74.3700 (cit. on p. 14).

[26] P. Eisenberger, P. M. Platzman, and H. Winick. "X-ray resonant Raman scattering: Observation of characteristic radiation narrower than the lifetime width". In: *Physical Review Letters* 36 (11 1976-03), pp. 623–626. ISSN: 00319007. DOI: 10.1103 /PhysRevLett.36.623 (cit. on p. 14).

[27] P. Indelicato, J. Bieroń, and P. Jönsson. "Are MCDF calculations 101% correct in the super-heavy elements range?" In: *Theoretical Chemistry Accounts* 129 (3-5 2011-06), pp. 495–505. ISSN: 1432881X. DOI: 10.1007/s00214-010-0887-3 (cit. on p. 14).

[28] P. Indelicato, O. Gorveix, and J. P. Desclaux. "Multiconfigurational Dirac-Fock studies of two-electron ions. II. Radiative corrections and comparison with experiment". In: *Journal of Physics B: Atomic and Molecular Physics* 20 (4 1987-02), p. 651. ISSN: 0022-3700. DOI: 10.1088/0022-3700/20/4/007 (cit. on p. 14).

[29] O. Gorceix, P. Indelicato, and J. P. Desclaux. "Multiconfiguration Dirac-Fock studies of two-electron ions. I. Electron-electron interaction". In: *Journal of Physics B: Atomic and Molecular Physics* 20 (4 1987-02), pp. 639–649. ISSN: 00223700. DOI: 10.1088/0022-3700/20/4/006 (cit. on p. 14).

[30] M. Guerra et al. "Fundamental Parameters Related to Selenium $K\alpha$ and $K\beta$ Emission X-ray Spectra". In: *Atoms* 9 (1 2021-01), p. 8. ISSN: 2218-2004. DOI: 10.3390/atoms9 010008. URL: https://www.mdpi.com/2218-2004/9/1/8 (cit. on pp. 14, 23).

[31] N. Paul et al. "Testing Quantum Electrodynamics with Exotic Atoms". In: *Physical Review Letters* 126 (17 2021-04), p. 173001. ISSN: 10797114. DOI: 10.1103 /PhysRevLett.126.173001 (cit. on p. 14).

[32] M. F. Gu. *The flexible atomic code*. 2008-05. DOI: 10.1139/P07-197 (cit. on p. 14).

[33]   P. Jönsson et al. "New version: Grasp2K relativistic atomic structure package". In: *Computer Physics Communications* 184 (9 2013-09), pp. 2197–2203. ISSN: 00104655. DOI: `10.1016/j.cpc.2013.02.016` (cit. on p. 14).

[34]   *ASCL.net - AUTOSTRUCTURE: General program for calculation of atomic and ionic properties.* URL: `https://ascl.net/1612.014` (cit. on p. 14).

[35]   J. P. Desclaux and P. Indelicato. *Input data for relativistic atomic program MCDF V 2019.1.* 2019 (cit. on p. 15).

[36]   *Metrology of simple systems and fundamental tests.* URL: `https://www.lkb.upmc.fr/metrologysimplesystems/mdfgme-a-general-purpose-multiconfiguration-dirac-foc-program/` (cit. on p. 15).

[37]   L. H. Thomas. "The calculation of atomic fields". In: *Mathematical Proceedings of the Cambridge Philosophical Society* 23.5 (1927), 542–548. DOI: `10.1017/S0305004100011683` (cit. on p. 21).

[38]   O. Tange. "GNU Parallel - The Command-Line Power Tool". In: *;login: The USENIX Magazine* 36.1 (2011), pp. 42–47. URL: `http://www.gnu.org/s/parallel` (cit. on p. 21).

[39]   D. Pinheiro et al. "K- and L-shell theoretical fluorescence yields for the Fe isonuclear sequence". In: *Radiation Physics and Chemistry* 203 (2023), p. 110594. ISSN: 0969-806X. DOI: `https://doi.org/10.1016/j.radphyschem.2022.110594`. URL: `https://www.sciencedirect.com/science/article/pii/S0969806X22006569` (cit. on p. 23).

[40]   P.-O. Löwdin. "Quantum Theory of Many-Particle Systems. I. Physical Interpretations by Means of Density Matrices, Natural Spin-Orbitals, and Convergence Problems in the Method of Configurational Interaction". In: *Phys. Rev.* 97 (6 1955), pp. 1474–1489. DOI: `10.1103/PhysRev.97.1474`. URL: `https://link.aps.org/doi/10.1103/PhysRev.97.1474` (cit. on p. 23).

[41]   T. Schoonjans et al. "The xraylib library for X-ray-matter interactions. Recent developments". In: *Spectrochimica Acta Part B: Atomic Spectroscopy* 66.11 (2011), pp. 776–784. ISSN: 0584-8547. DOI: `https://doi.org/10.1016/j.sab.2011.09.011`. URL: `https://www.sciencedirect.com/science/article/pii/S0584854711001984` (cit. on p. 32).

[42]   R. Deslattes et al. *X-ray Transition Energies (version 1.2).* 2005. DOI: `https://dx.doi.org/10.18434/T4859Z`. URL: `http://physics.nist.gov/XrayTrans` (visited on 2023-09-09) (cit. on p. 32).

[43]   T. pandas development team. *pandas-dev/pandas: Pandas.* Version latest. 2020-02. DOI: `10.5281/zenodo.3509134`. URL: `https://doi.org/10.5281/zenodo.3509134` (cit. on p. 41).

[44] W. E. Lamb and R. C. Retherford. "Fine structure of the hydrogen atom by a microwave method". In: *Physical Review* 72 (3 1947-08), pp. 241–243. ISSN: 0031899X. DOI: 10.1103/PhysRev.72.241 (cit. on p. 52).

The Breit Hamiltonian Operators

Note: This operators are valid for the electrons in an atom.

The free particle energy:

$$H_0 = \sum_i^N \frac{p^2}{2m_e} \tag{A.1}$$

The electron-nucleus Coulomb attraction:

$$H_1 = \sum_i^N -\frac{e^2 Z}{r_i} \tag{A.2}$$

The electron-electron Coulomb repulsion:

$$H_2 = \sum_{i<j} \frac{e^2}{r_{ij}} \tag{A.3}$$

Incorporates the relativistic apparent mass - velocity dependance:

$$H_3 = -\frac{1}{8m_e{}^3 c^2} \sum_i^N p_i^4 \tag{A.4}$$

Electric field retardation and magnetic dipole interaction:

$$H_4 = -\frac{e^2}{2m_e{}^2 c^2} \sum_{i<j} \left[\frac{p_i \cdot p_j}{r_{ij}} + \frac{\left(r_{ij} \cdot p_{ij}\right)\left(r_{ij} \cdot p_j\right)}{r_{ij}{}^3} \right] \tag{A.5}$$

Darwin's term, accounts for the electron's quantum fluctuation motion:

$$H_5 = \frac{\pi e \hbar^2}{2m_e{}^2 c^2} \sum_{i<j} \frac{Z}{2} \left[\delta(r_i) + \delta(r_j) \right] + \delta(r_{ij}) \tag{A.6}$$

And the last two operators, for the consideration of spin orbit interactions:

$$H_6 = \frac{e^2 \hbar^2}{2 m_e{}^2 c^2} \sum_{i<j} \left(Z \frac{\boldsymbol{r}_i \times \boldsymbol{p}_i}{r_i{}^3} - \frac{\boldsymbol{r}_{ij} \times \boldsymbol{p}_i}{r_{ij}{}^3} + 2 \frac{\boldsymbol{r}_{ij} \times \boldsymbol{p}_j}{r_{ij}{}^3} \right) \boldsymbol{s}_i + \left(Z \frac{\boldsymbol{r}_j \times \boldsymbol{p}_j}{r_j{}^3} - \frac{\boldsymbol{r}_{ji} \times \boldsymbol{p}_j}{r_{ij}{}^3} + 2 \frac{\boldsymbol{r}_{ji} \times \boldsymbol{p}_i}{r_{ij}{}^3} \right) \boldsymbol{s}_j$$

$$\text{(A.7)}$$

$$H_7 = \frac{e^2 \hbar^2}{m_e{}^2 c^2} \sum_{i<j} \left(-\frac{8\pi}{3} \boldsymbol{s}_i \cdot \boldsymbol{s}_j \, \delta(\boldsymbol{r}_{ij}) + \frac{1}{r_{ij}{}^3} \left[\boldsymbol{s}_i \cdot \boldsymbol{s}_j - \frac{3(\boldsymbol{s}_i \cdot \boldsymbol{r}_{ij})(\boldsymbol{s}_j \cdot \boldsymbol{r}_{ij})}{r_{ij}{}^2} \right] \right) \qquad \text{(A.8)}$$
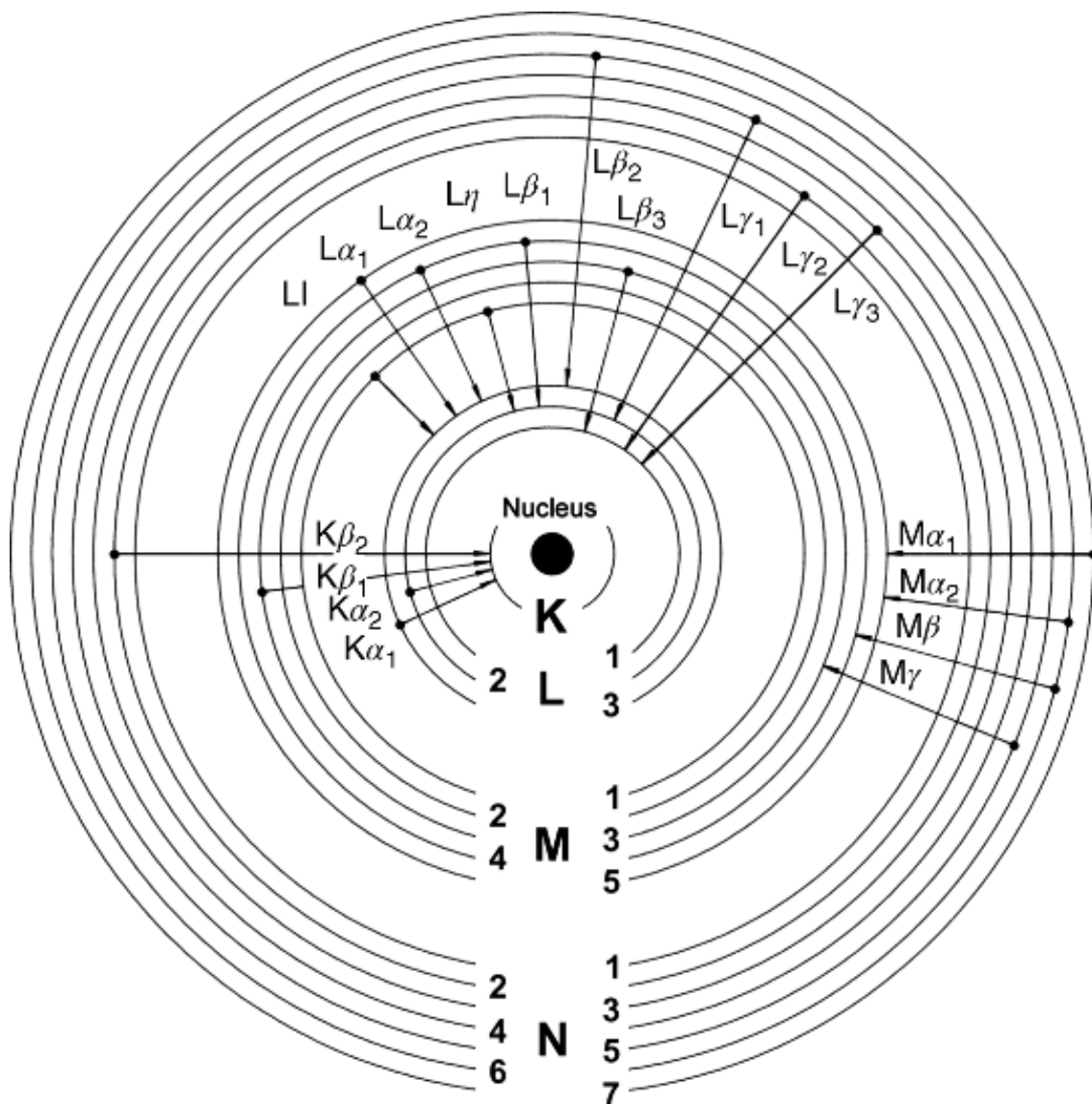
Transition Diagram

Figure B.1: Transition notation scheme. Adapted from [2]

QED considerations

It should be apparent by now that studying Atomic systems call not only for relativistic effects and corrections, but also for QED ones.

One of the most famous cases where QED came to light was the discovery of the Lamb Shift [44], when it was discovered Hydrogen's $2s_{1/2}$ and $2p_{1/2}$ levels were in fact, not degenerate (did not have the same energy), contrary to what was expected from solving Dirac's equation. This difference in energy came to be known as the Lamb Shift, only explained by QED effects.

C.1 Self-Energy

The self-energy represents a particle's emission and reabsorption of virtual photon, present in the particle's own generated field. This interaction has the most impact in the Lamb Shift effect and when performing energy corrections. One of its Feynman Diagrams can be seen in Figure C.1a.

C.2 Vacuum Polarization

As previously stated, electromagnetic fields, such as the Coulomb field generated by the nucleus, are mediated by virtual photons. These photons can lead to the creation of electron-positron pairs which create screening effects. Pair annihilation will follow, leading to the production of another virtual photon (Figure C.1b).

(a) Self Energy

(b) Vacuum Polarization

Figure C.1: QED Feynman Diagrams

4p excited Copper configurations

I.1 1-hole configurations

```
1    (1s)1 (2s)2 (2p)6 (3s)2 (3p)6 (4s)1 (3d)10 (4p)1  ,1s
2    (1s)2 (2s)1 (2p)6 (3s)2 (3p)6 (4s)1 (3d)10 (4p)1  ,2s
3    (1s)2 (2s)2 (2p)5 (3s)2 (3p)6 (4s)1 (3d)10 (4p)1  ,2p
4    (1s)2 (2s)2 (2p)6 (3s)1 (3p)6 (4s)1 (3d)10 (4p)1  ,3s
5    (1s)2 (2s)2 (2p)6 (3s)2 (3p)5 (4s)1 (3d)10 (4p)1  ,3p
6    (1s)2 (2s)2 (2p)6 (3s)2 (3p)6 (4s)1 (3d)9 (4p)1   ,3d
7    (1s)2 (2s)2 (2p)6 (3s)2 (3p)6 (3d)10 (4p)1        ,4s
8    (1s)2 (2s)2 (2p)6 (3s)2 (3p)6 (4s)1 (3d)10        ,4p
```

I.2 2-holes configurations

```
1    (2s)2 (2p)6 (3s)2 (3p)6 (3d)10 (4s)1 (4p)1        ,1s_1s
2    (1s)1 (2s)1 (2p)6 (3s)2 (3p)6 (3d)10 (4s)1 (4p)1  ,1s_2s
3    (1s)1 (2s)2 (2p)5 (3s)2 (3p)6 (3d)10 (4s)1 (4p)1  ,1s_2p
4    (1s)1 (2s)2 (2p)6 (3s)1 (3p)6 (3d)10 (4s)1 (4p)1  ,1s_3s
5    (1s)1 (2s)2 (2p)6 (3s)2 (3p)5 (3d)10 (4s)1 (4p)1  ,1s_3p
6    (1s)1 (2s)2 (2p)6 (3s)2 (3p)6 (3d)9 (4s)1 (4p)1   ,1s_3d
7    (1s)1 (2s)2 (2p)6 (3s)2 (3p)6 (3d)10 (4p)1        ,1s_4s
8    (1s)1 (2s)2 (2p)6 (3s)2 (3p)6 (3d)10 (4s)1        ,1s_4p
9    (1s)2 (2p)6 (3s)2 (3p)6 (3d)10 (4s)1 (4p)1        ,2s_2s
10   (1s)2 (2s)1 (2p)5 (3s)2 (3p)6 (3d)10 (4s)1 (4p)1  ,2s_2p
11   (1s)2 (2s)1 (2p)6 (3s)1 (3p)6 (3d)10 (4s)1 (4p)1  ,2s_3s
12   (1s)2 (2s)1 (2p)6 (3s)2 (3p)5 (3d)10 (4s)1 (4p)1  ,2s_3p
13   (1s)2 (2s)1 (2p)6 (3s)2 (3p)6 (3d)9 (4s)1 (4p)1   ,2s_3d
14   (1s)2 (2s)1 (2p)6 (3s)2 (3p)6 (3d)10 (4p)1        ,2s_4s
15   (1s)2 (2s)1 (2p)6 (3s)2 (3p)6 (3d)10 (4s)1        ,2s_4p
16   (1s)2 (2s)2 (2p)4 (3s)2 (3p)6 (3d)10 (4s)1 (4p)1  ,2p_2p
17   (1s)2 (2s)2 (2p)5 (3s)1 (3p)6 (3d)10 (4s)1 (4p)1  ,2p_3s
18   (1s)2 (2s)2 (2p)5 (3s)2 (3p)5 (3d)10 (4s)1 (4p)1  ,2p_3p
19   (1s)2 (2s)2 (2p)5 (3s)2 (3p)6 (3d)9 (4s)1 (4p)1   ,2p_3d
20   (1s)2 (2s)2 (2p)5 (3s)2 (3p)6 (3d)10 (4p)1        ,2p_4s
21   (1s)2 (2s)2 (2p)5 (3s)2 (3p)6 (3d)10 (4s)1        ,2p_4p
```

```
22    (1s)2 (2s)2 (2p)6 (3p)6 (3d)10 (4s)1 (4p)1        ,3s_3s
23    (1s)2 (2s)2 (2p)6 (3s)1 (3p)5 (3d)10 (4s)1 (4p)1 ,3s_3p
```

First cycle template

```
1    program_year=2019 program_version=1
2    *   1 mcdfgmelabel
3        scfmdf max  :
4        mod_lightspeed=n
5        nz=mcdfgmeatomicnumber
6        mdf  opt_ener=todo  modfilname_ener=n modfilname_wf=n do_scf=y
7        Breit=full  mag_scf=y  ret_scf=y
8        qedstpg_n4=n
9        vacpol_scf=y
10       energy
11   #    use_mcdfener=y
12   #    opt_relax=y
13       ret_Lorentz=y
14       opt_qedel=y :
15   # ":" above is for ilams taken to be the default value
16       mod_mesh=n
17   #    hx=0.012 r(1)=0.001 amesh=0.01 :
18       exotic=n
19       use_nms=y
20       mod_nuc=n
21       project=n
22   #    cgt_order_vint=y order=6
23       cgt_order_vint=n
24       def_config=given
25       nbel=mcdfgmeelectronnb jjt=mcdfgmejj  :
26   c  1 mcdfgmeconfiguration:
27   end
28   # initial state parameters
29       neigv=mcdfgmeneigv   icmul=0   iprfgr=0
30       norbsc=00  ndep=0   nlec=0   nec=1  :
31       nstep=0
32       lregul=n  modtest=n
33       modsolv_orb=n
34       mod_odlm=n
35   # data for uwfrdf
```

```
36          :
37      **
```

Input File .f05 Example

```
1    program_year=2019 program_version=1
2    *   1 mcdfgmelabel
3        scfmdf max  :
4        mod_lightspeed=n
5        nz=mcdfgmeatomicnumber
6        mdf  opt_ener=todo  modfilname_ener=n modfilname_wf=n do_scf=y
7        Breit=full  mag_scf=y  ret_scf=y
8        qedstpg_n4=n
9        vacpol_scf=y
10       energy
11   #    use_mcdfener=y
12   #    opt_relax=y
13       ret_Lorentz=y
14       opt_qedel=y :
15   # ":" above is for ilams taken to be the default value
16       mod_mesh=n
17   #    hx=0.012 r(1)=0.001 amesh=0.01 :
18       exotic=n
19       use_nms=y
20       mod_nuc=n
21       project=n
22   #    cgt_order_vint=y order=6
23       cgt_order_vint=n
24       def_config=given
25       nbel=mcdfgmeelectronnb jjt=mcdfgmejj  :
26   c  1 mcdfgmeconfiguration:
27   end
28   # initial state parameters
29       neigv=mcdfgmeneigv   icmul=0   iprfgr=0
30       norbsc=00  ndep=0  nlec=0   nec=1  :
31       nstep=10
32       n y y  50  z=mcdfgmeatomicnumber  1.D-2  0.2  1.  1.
33       n y y  50  z=mcdfgmeatomicnumber  3.D-3  0.2  1.  1.
34       n y y  50  z=mcdfgmeatomicnumber  1.D-3  0.3  1.  1.
35       n y y  50  z=mcdfgmeatomicnumber  3.D-4  0.3  1.  1.
```

```
36      n y y  50   z=mcdfgmeatomicnumber  1.D-4  0.5  1.  1.
37      n y y  50   z=mcdfgmeatomicnumber  3.D-5  0.5  1.  1.
38      n y y  50   z=mcdfgmeatomicnumber  1.D-5  0.5  1.  1.
39      n y y  100  z=mcdfgmeatomicnumber  4.D-6  1.  1.  1.
40      n y y  100  z=mcdfgmeatomicnumber  2.D-6  1.  1.  1.
41      n y y  200  z=mcdfgmeatomicnumber  1.D-6  1.  1.  1.
42   lregul=n  modtest=n
43   modsolv_orb=n
44   mod_odlm=n
45 # data for uwfrdf
46   :
47 **
```

2023 X-ray resonant Raman scattering: Spectra simulation from first principles for Copper bellow ionization threshold using high-performance computing   Gonçalo Baptista